UPCommons

Portal del coneixement obert de la UPC

An Immersed Boundary method to conjugate heat transfer problems in complex geometries. Application to an automotive antenna

F. Favre[a,b], O. Antepara[a,c], C. Oliet[a], O. Lehmkuhl[a], C.D. Perez-Segarra[a]

[a]*Heat and Mass Transfer Technological Center (CTTC), Universitat Politècnica de Catalunya - BarcelonaTech (UPC) ESEIATT, Colom 11, 08222 Terrassa (Barcelona), Spain*
[b]*Instituto de Ingeniería Mecánica y Producción Industrial (IIMPI), Universidad de la República, Uruguay*
[c]*TermoFluids S.L., Avda Jacquard 97 1-E, 08222 Terrassa (Barcelona), Spain*

Abstract

Considering that the most common reason for electronic component failure is the excessive temperature level, an efficient thermal management design can prolong the operating life of the equipment, while also increasing its performance. Computational Fluid Dynamics and Heat Transfer (CFD&HT) have proved valuable in the study of these problems, since they can produce reliable fields of fluid flow, temperature and heat fluxes. Moreover, thanks to the recent advances in high-performance computers, CFD&HT numerical simulations are becoming viable tools to study real problems. The conventional approach, which consists of employing body-conformal meshes to the solids and fluids regions, often results costly and ineffective in applications with very complex geometries and large deformation. For these cases, an alternative approach, the Immersed Boundary Method (IBM), which employs a non-body conformal mesh and discretizes the entire domain using a special treatment in the vicinity of the solid-fluid interfaces, has proven more effective. In this work, an IBM was extended to simulate problems with conjugate heat transfer (CHT) boundary conditions taking into account the radiative exchange between surfaces. It was designed to work with any type of mesh (domain discretization) and to handle any body geometry. The implementation was validated and verified by several simulations of benchmark cases. Moreover, the IBM was applied in an industrial application which consists of the simulation of a Smart Antenna Module (SAM). All in all, the carried out studies resulted in a monolithic methodology for the simulation of realistic situations, where all three heat transfer mechanisms can be considered in complex geometries.

1. Introduction

The trend for decreasing the size of electronic components, but increasing its power consumption, originates a challenge to develop effective thermal dissipation solutions. The most common reason for failure of electronic components is the temperature rise. Therefore, an efficient design to remove the generated heat maintaining a control of the temperature can prolong the useful life of the equipment and increase its

performance. The traditional strategy used to study the complex phenomena involved in cooling electronics, i.e. the fluid-dynamics issues, heat conduction in solids and radiative exchange between surfaces, consists of experimentation with physical prototypes. Nowadays, thanks to the increase of computational power, as well as the improvement of mathematical and numerical algorithms, the experimental techniques can be supported by a wide range of effective numerical procedures. In particular, Computational Fluid Dynamics and Heat Transfer (CFD&HT) can produce reliable fields of fluid flow, temperature and heat fluxes, useful in the design process in order to minimize the costs of producing a large number of prototypes. Aydin et al. [1] studied numerically a rectangular two-dimensional enclosure with localized heating from below. Panthalookaran [2] has performed an optimization of cooling electronics based on CFD. Boukhanouf and Haddad [3] presents results of CFD analysis of an electronic cooling enclosure used as a part of a telecommunication system. Semen et al. [4] have simulated the problem of conjugate natural convection combined with surface thermal radiation in a two-dimensional enclosure, and also in three-dimensional enclosures [5, 6]. Riaz et al. [7] have optimized a naturally air-cooled electronic equipment using CFD.

The above mentioned studies use the traditional body-conformal approach, where the computational domain is discretized conformal to the solid walls of the enclosures solving simple geometries. It is well known that the mesh generation procedure is a very demanding task for intricate geometries. In the past few years the Immersed Boundary method (IBM) have gained a special interest as an alternative to the body-conformal mesh methods. They allow to highly simplify the mesh generation procedure because cartesian meshes can be applied. Whilst on a body-conformal mesh, the boundary condition is imposed directly. In an IBM it is imposed by the modification of the discretized Navier-Stokes (NS) equations, generally by including a forcing term. Depending on how the forcing term is defined, the IBM is classified into two categories [8]: continuous forcing approach and the discrete forcing approach.

The original IBM introduced by Peskin [9] in 1972, corresponds to the continuous approach. In that work, the immersed boundary is represented by a series of Lagrangian markers linked by springs, which exert a singular force on the fluid by a discretized approximation to the Dirac delta function. It has been applied in a number of problems, i.e. biological flows [9–12] with elastic boundaries. It has also been used for rigid boundaries by increasing the stiffness of the body [13]. However, this approach can lead to stability problems.

The discrete forcing approach was introduced by Mohd-Yusof [14] in a spectral method and applied by Fadlun et al. [15] using a finite difference method. In this case, the forcing is defined in the discrete space by imposing the boundary condition into the solution. This process can be seen as a reconstruction procedure. In fact, in [15] the forcing is not evaluated explicitly. This methodology allows a sharp representation of the immersed boundary and is well suited for rigid boundaries. For these reasons, this approach has been taken in the present work. This technique has been widely used in the past years, with small differences in the reconstruction schemes. In [15–17], the solution is reconstructed in the fluid nodes closest to the immersed boundary. In [18–20], the boundary condition is enforced through the so-called ghost cells, nodes located in the solid and closest to the solid-fluid boundary, where a extrapolated value of velocity is imposed.

The IBM formulation can be naturally extended to thermal problems by introducing a source term in the energy equation. Following this idea, several works are available in the literature that simulates heat transfer problems with the usual boundary conditions of constant temperature (Dirichlet) [21, 22] and both, Dirichlet and constant heat flux (Neumann) [23–27]. In several applications the CHT problem has to be solved, which means that the energy equation in the interior of the solid must be coupled with the analysis of the fluid flow. There are relatively few works that address this problem. One of the first implementation of this condition with the IBM was by Iaccarino and Moreau [28]. They developed a reconstruction procedure for the temperature field at both sides of the interface. More recently, Kang et al. [29] and Nagendra et al. [30] proposed similar approaches based on interpolation techniques, for cartesian and curvilinear grids respectively.

2

Instead of using a reconstruction procedure, Sato et al. [31] developed a consistent discretization scheme for a cartesian grid method. Similar to that, the present work aims to develop a modification procedure of the convective and diffusive operators that consider the presence of solids, which modifies the heat transfer calculation instead of reconstructing the temperature field in the interface. To do so, mass fluxes at the faces in the vicinity of the solid must be carefully computed to have an accurate convective term. In the present implementation, a boundary condition to the pressure field is imposed to ensure that no mass passes through the bodies. Galione et al. [32] use this idea for their fixed-grid modelisation of melting and solidification by modifying the Poisson equation. For IBM problems, a similar approach can be taken using a cut cell based discretization [33, 34] only in the Poisson equation as in [35].

It is well-known that radiative exchange between surfaces can impact considerably on the solution of particular problems, even in low-temperature application such as cooling electronics. Different papers have been presented in the literature [4, 6, 36–39] considering CHT problems with radiation and using body-conformal meshes in relatively simple geometries. However, the non-body conformal methods developed to simulate CHT problems mentioned above [28–31] neglect radiation effects. In the present work, a source term is added in the energy equation to introduce the radiative effect. This source term is computed after solving the net radiation problem.

Summarizing, the aims of the current model are: (*i*) to extend the IBM to explicitly impose a wall boundary condition to the pressure field to ensure the non-slip condition, (*ii*) to extend the IBM for CHT problems, and (*iii*) to include the radiation between surfaces in the formulation. The developed methodology is used to study the thermal behaviour of a Smart Antenna Module. A SAM is a car component that combines antenna elements and radio receivers in one package, including a printed circuit board (PCB) with the electronics needed for a number of applications, i.e. GPS, WiFi, emergency calls, etc. This is a problem with many objects with intricate geometries, where the body-conformal approach requires the generation of a large number of complex meshes. Using the IBM approach, a detailed thermal analysis of the SAM was carried out, testing numerous configurations in a more simple way. An hexahedral mesh is employed, which is easy to generate. The near-body regions are then automatically refined using local mesh refinement [40].

The paper is organized as follows. The mathematical and numerical details of the methodology are presented in Section 2. The method is validated and verified in Section 3. An accuracy study is performed, a numerical test is carried out to evaluate the Poisson modification and an example case is solved, comparing the solution with reference data obtained by a body-conformal approach. The thermal performance study of a SAM is included in Section 4. Finally, the conclusions are presented in section 5.

2. Mathematical and Numerical formulation

In this section we first present the basis of the method developed to simulate conjugate heat transfer problems. Next, we focus on the special treatment which we apply because of the non-body conformal approach. This is the velocity field reconstruction in the vicinity of the bodies, the pressure-velocity decoupling procedure and the modifications introduced in the discretization of the energy equation.

2.1. Governing equations

The classic Navier-Stokes equations, expressing mass and momentum equation using the Boussinesq approximation, and the energy balance discretized can be written in matrix form as,

$$Mu = 0 \tag{1}$$

$$\Omega\frac{\partial u}{\partial t} = -C\left(u\right)u + \nu Du + \rho^{-1}Gp + \beta g(T - T_0) + f_{IB} \tag{2}$$

$$\Omega\frac{\partial T}{\partial t} = -C\left(u\right)T + \frac{\lambda}{\rho c_P}DT + s_{IB} \tag{3}$$

where M, $C\left(u\right)$, D and G are the divergence, convective, diffusive and gradient operators respectively, Ω is a diagonal matrix with the sizes of control volumes, T is the temperature, p represents the pressure, u is the velocity, β is the coefficient of thermal expansion, g is the gravity vector, T_0 is a reference temperature, f_{IB} and s_{IB} are the forcing and source terms included due to the immersed boundaries and ρ, ν, λ, c_P are the density, the kinematic viscosity, the thermal conductivity and the specific heat of the fluid.

In the present work, a Computational Fluid Dynamics (CFD) software package, TermoFluids [41], was used as a solver of momentum and energy equations. The IBM was incorporated in this package as detailed later. The governing equations have been discretized on a collocated unstructured grid arrangement by means of second-order, spectro-consistent schemes. The conservative nature of these schemes ensures the preservation of the symmetry properties of the continuous differential operators.

A non-body conformal approach is used to study the problem of the flow around a solid body presented in Figure 1. Therefore, the entire domain ($\Omega_f \cup \Omega_s$) is discretized by a volumetric mesh called the Eulerian mesh. The boundary of the body is represented by an unstructured surface mesh, composed by a series of triangles in stereo-lithography (STL) format [42], called the Lagrangian mesh. The governing equations are discretized in the Eulerian mesh, and forcing and source terms are included in the vicinity of Γ_s in order to impose the immersed boundary conditions.
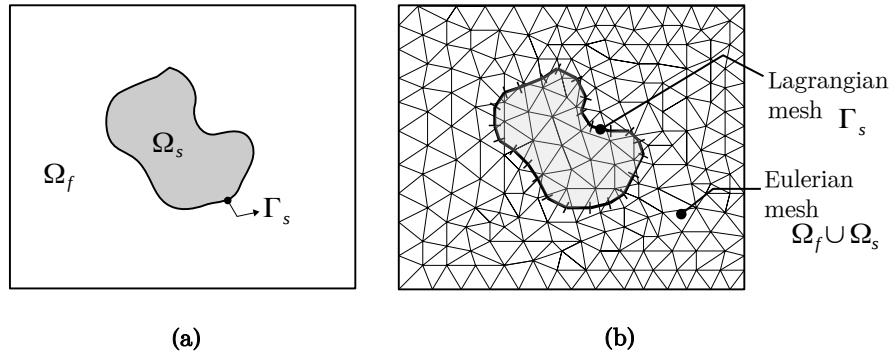

Figure 1: (a) Schematic representation of the problem of a generic body immersed in a fluid flow. (b) Discretization: Eulerian mesh to discretize the entire domain ($\Omega_f \cup \Omega_s$); Lagrangian mesh to represent the immersed boundary (Γ_s).

These forcing and source terms are included to enforce the immersed boundary conditions in momentum and energy equation, respectively. They affect the nodes in the vicinity and in the interior of the immersed bodies. Therefore, once the Eulerian mesh is defined, and nodes are located at the centroid of the control volume, they are classified as: interior points, interior forcing points, exterior forcing points and exterior points. The exterior forcing points are nodes that are outside and meet one or both of these conditions: (i) The node has a neighbour which is inside the object. (ii) Their cell-volume is cut by the immersed boundary.

In the specific case of a node located on the solid-fluid interface, it is considered in general as a forcing

point. Analogue to the exterior forcing points, we define the interior forcing points. For this case, the node is in the interior and its neighbours are on the exterior of the objects. The remaining nodes are the so-called interior or exterior points according to its location. The different type of nodes are clearly identified in Figure 2.
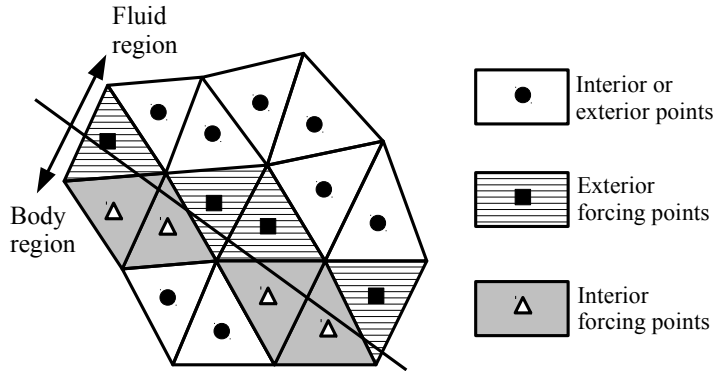

Figure 2: Example of Control Volumes intersected by an object: ($\bullet$) Interior or Exterior Points; ($\blacksquare$) Exterior Forcing Points; ($\triangle$) Interior Forcing Points. Differentiation between interior and exterior forcing points.

The methods used to reconstruct the velocity field in the vicinity of the body, modify the pressure-velocity decoupling, and adapt the discretization of the energy equation conform the special methodology developed in this work to simulate conjugate heat transfer. They are described as follows.

2.2. Velocity field reconstruction

A fractional-step method is employed to perform the time integration of the equations. The convective and diffusive terms are explicitly treated with a self adaptive strategy using the $\kappa 1L2$ method [43, 44]. This time-integration scheme can be viewed as an optimization of the classical second-order Adams-Bashforth (AB2) scheme ($\kappa = 1/2$), for further details see [43, 44].

In the framework of an IBM, first a provisional predictor velocity field is computed, not taking into account the presence of the immersed boundaries ($f_{IB} = 0$). The predictor velocity field is then reconstructed in the interior and forcing points in order to impose the immersed boundary conditions. This procedure is possible only in an explicit time integration. For a prescribed movement of the body, the velocities $\vec{V}$ of the interior and interior forcing points are directly calculated from their coordinates. However, to compute the exterior forcing points velocities $\vec{V}_{fp}$ some approximation has to be used because, by definition, these nodes are outside the object. According to Fadlun et al. [15], the global accuracy of the scheme is maintained when a second-order interpolation is used to calculate $\vec{V}_{fp}$.

Following this approach, equation (4) is used to estimate $\vec{V}_{fp}$:

$$\vec{V}_{fp} = \vec{V}^{n+1}(\vec{X}_S) \quad + \quad a_1(\vec{u}_{nb1}^p - \vec{V}^{n+1}(\vec{X}_S)) + a_2(\vec{u}_{nb2}^p - \vec{V}^{n+1}(\vec{X}_S))$$
$$+ \quad a_3(\vec{u}_{nb3}^p - \vec{V}^{n+1}(\vec{X}_S)) \tag{4}$$

where a_i are the interpolation coefficients, and four velocities are used: one refers to the velocity $\vec{V}(\vec{X}_S)$ of the closest point of the object and the other three $\vec{u}_{nbi}^p$ are the predictor velocities of exterior nodes. A

scheme of the points considered is presented in Figure 3, where $\vec{X}_{fp}$ is the position of the forcing point, $\vec{X}_S$ is the closest point on the body, and $\vec{X}_{nbi}$ are the locations of the exterior nodes nb_i.
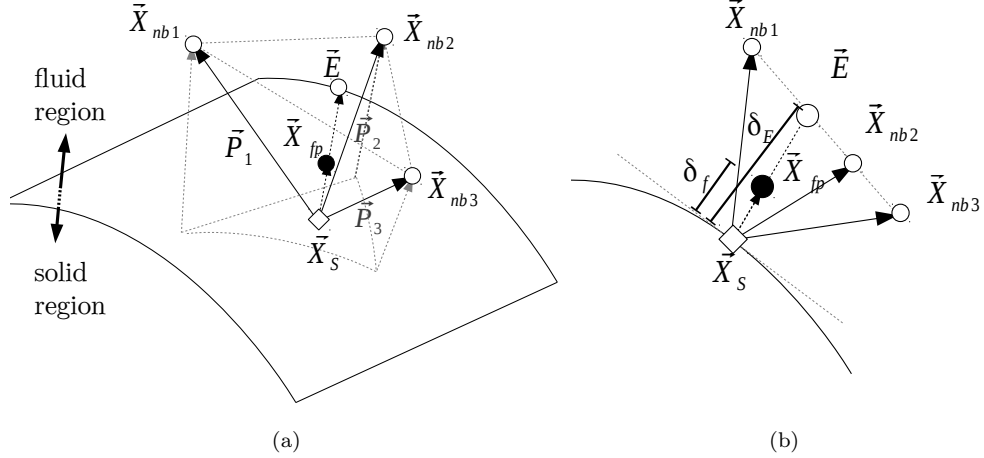

Figure 3: (a) Interpolation scheme: ($\Diamond$) Nearest point on the body to the forcing point; ($\bullet$) Forcing point; ($\circ$) Selected neighbours to the interpolation. (b) Two-dimensional view.

To perform the interpolation of equation (4), the coefficients a_i must be computed and a set of three exterior nodes of the Eulerian mesh has to be selected.

To calculate a_i only geometric data is needed. To do so, the following vectors are defined:

$$
\begin{align}
\vec{P}_i &= \vec{X}_{nbi} - \vec{X}_S, \quad i = 1, 2, 3 \tag{5} \\
\vec{P}_{fp} &= \vec{X}_{fp} - \vec{X}_S \tag{6}
\end{align}
$$

A 3×3 matrix A is then constructed using the vectors $\vec{P}_i$. Finally, the inverse of the matrix A multiplied by the vector $\vec{P}_{fp}$ results in the coefficients for the interpolation:

$$
\begin{align}
A &= [\vec{P}_1 \vec{P}_2 \vec{P}_3] \tag{7} \\
(a_1, a_2, a_3) &= A^{-1} \vec{P}_{fp} \tag{8}
\end{align}
$$

$$
\tag{9}
$$

To select the set of three exterior nodes that will be used in the interpolation, all the exterior neighbours of the forcing point are considered. The criteria used to select a particular combination aims to: (i) avoid extrapolations, which could produce numerical instabilities and lower global accuracy, and (ii) minimize the distance from the neighbors location $\vec{X}_{nbi}$ to the point $\vec{X}_S$.

The first condition is accomplished considering only the combinations which produce coefficients a_i between 0 and 1. This is equivalent to say that the forcing point is contained inside the tetrahedron defined by the four points used in the interpolation. To take into account the second condition, the set of neighbours (nb_j, nb_k, nb_l) which minimize:

6

$$Norm(nb_j, nb_k, nb_l) = (\vec{P}_j \cdot \vec{P}_j + \vec{P}_k \cdot \vec{P}_k + \vec{P}_l \cdot \vec{P}_l)^{0.5} \tag{10}$$

will be the one selected.

The procedure employed to select the neighbours and to compute the interpolation coefficients a_i, does not consider any structure of the mesh. Therefore, it could be applied to both structured and unstructured meshes.

Must be noted that in a explicit time integration methodology, there is no need to actually compute the forcing term f_{IB}.

2.3. Pressure-Velocity decoupling procedure

The forcing term is applied to the predictor velocity field, which also affects the pseudo mass at the faces. After solving the Poisson equation, the predictor velocity and pseudo mass are then corrected, obtaining the real velocity and mass fields which do not verify exactly the immersed boundary conditions. Some non-physical mass flux is going to pass through the solids.

Despite this, the solver presents a second-order accuracy and the quality of the solution for several cases is good (not shown here). However, there are many cases where this error could be appreciable. For example, the flow around a baffled channel with very thin baffles generates a big pressure difference between the sides of the baffle. If the baffle is represented as an immersed boundary, the big pressure gradient in its interior could produce a considerable mass passing through it. In section 3.2, this case will be used to show this effect and test possible improvements.

To avoid this error and ensure no mass passing through the bodies, the pressure-velocity decoupling procedure is solved with an approach based on the cut-cell method. The finite-volume integration of Poisson equation for a cell k are then written as:

$$\sum_{f \epsilon \mathcal{F}(k)} (\nabla p)_f^{n+1} \cdot \vec{n}_f A_f = \frac{1}{\Delta t} \sum_f \dot{m}_f^p \tag{11}$$

$$\vec{u}_k^{n+1} = \vec{u}_k^p - \frac{\Delta t}{\rho V_k} \sum_f (p_f^{n+1} \vec{n}_f) A_f \tag{12}$$

$$\dot{m}_f^{n+1} = \dot{m}_f^p - \Delta t (\nabla p)_f^{n+1} \cdot \vec{n}_f A_f \tag{13}$$

where $\mathcal{F}(k)$ are the faces of the cell k, V_k is the volume of the cell k, A_f is the surface of a face f, the subscript k refers to the cell itself, and the subscript f refers to the faces of the cell.

The pseudo mass $\dot{m}_f^p$ is computed with a reconstruction approach, and the coefficients of the matrix for the interior cells and cut cells are modified based on geometric information. Moreover, a virtual cell-merging technique [35] is used to modify the independent term of the equation (11). The details are presented as follows:

2.3.1. Pseudo Mass reconstruction

For a better estimation of the pseudo mass in the vicinity of the immersed bodies, a reconstruction procedure analogue to the one used for the predictor velocity is now employed. It consists of cutting the faces to distinguish the fluid section of the face from the solid one. Each face intersected by an immersed boundary is divided into a fluid-face with surface A_f^F, and a solid-face with surface A_f^S (see Figure 4).

The centroid of the fluid face and it projection to the Lagrangian mesh are computed. The predictor velocity at the centroid of the fluid face, $\vec{u}_f^p$, is then calculated by linear interpolation using the projected point and three neighbours. The procedure to do that is the same used for the forcing points (see section 2.2). Finally, the pseudo mass is determined using the surface of the fluid face as follows:

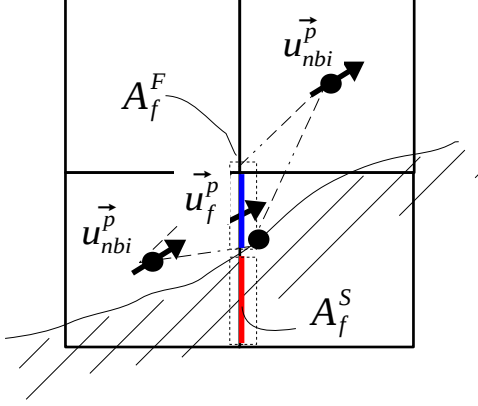$$\dot{m}_f^p = \rho \vec{u}_f^p \vec{n}_f^F A_f^F \tag{14}$$

Figure 4: Example of Control Volumes intersected by an object. Scheme of the method to compute the pseudo mass in cut faces.

2.3.2. Poisson modification

We can distinguish two types of cut cells. The ones with the node in the fluid region, generally called regular cut cells, and the ones with the node in the solid, called small cut cells, because the fluid fraction of it could be arbitrarily small. Both types of cells are shown in Figure 5, marked with blue dash lines the regular cut cells and with red dashed lines the small cut cells. To ensure a good-conditioned Poisson equation, the small cells are treated differently.

The conventional finite-volume discretization for equations (11), (12) and (13) described in [34] is used for a regular cut cell k (see Figure 5):

$$\dot{m}_{IB}^p A_{IB} + \sum_{f \epsilon \mathcal{F}(k)} \dot{m}_f^p \;=\; \Delta t \left((p_{IB}^{n+1} - p_k^{n+1}) \frac{A_{IB}}{\delta d_{IB}} + \sum_f \left(p_{nb}^{n+1} - p_k^{n+1} \right) \frac{a_f^F A_f}{\delta d_f} \right) \tag{15}$$

$$\vec{u}_k^{n+1} \;=\; \vec{u}_k^p - \frac{\Delta t}{\rho \gamma V_k} \left(p_{IB}^{n+1} \vec{n}_{IB}^F A_{IB} + \sum_f p_f^{n+1} \vec{n}_f^F a_f^F A_f \right) \tag{16}$$

$$\dot{m}_f^{n+1} \;=\; \dot{m}_f^p - \Delta t a_f^F A_f \frac{(p_{nb}^{n+1} - p_k^{n+1})}{\delta d_f} \tag{17}$$

where $a_f^F = A_f^F / A_f$ is the fluid surface fraction of the face f and $\gamma = V_k^F / V_k$ is the volume fraction of the cell k. The subscript IB refers to the section of the immersed boundary intersected by the cell k called ∂IB, A_{IB} is its surface, δd_{IB}, is the distance between the node of k and ∂IB and p_{IB} is the pressure at that location.
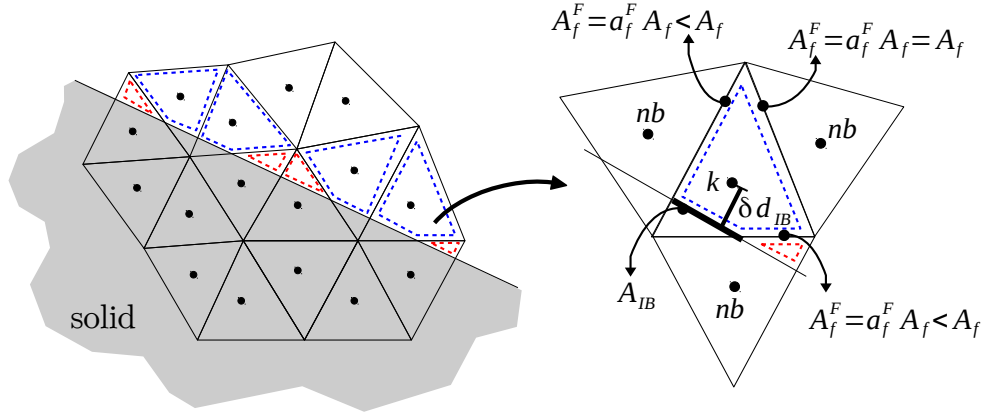
8

Figure 5: Definition of regular cut-cells and small cut-cells.

The subscript nb refers to the face-neighbour of k, and δd_f is the normal-projected distance between the nodes k and nb. For the cells which are not cut by an immersed boundary, all the coefficients a_f^F and γ are equal to 1. Therefore, the discretization corresponds to the classic second-order, spectro-consistence scheme used in TermoFluids [41].

2.3.3. Virtual cell merging technique

As stated earlier, small cells are treated with a different approach. Since they can be arbitrarily small, use the same approach than for the regular cut cells could lead to an ill-conditioned pressure Poisson equation. Small cut cells can also cause viscous stability problems. To avoid both problems, Ye et al. [34] and Udaykumar et al. [33] geometrically merge the small cells with its regular neighbours. This approach eliminates small cells, but is highly complex and computationally expensive, because what they do is recompute the mesh. In the present work a slightly different methodology is implemented, the so called virtual cell merging technique. It was first proposed by Meyer et al. [45] for momentum equation, and adapted by Seo and Mittal [35] for the pressure Poisson equation.

The technique consists of modifying the independent term of the Poisson equation. First, the independent terms $b(k) = \sum_f \dot{m}_f^P$ are computed for every cell, including the small ones. After that, the term b_{small} of each small cells is transferred to its regular neighbours. This means that the term b_{nb} of each regular neighbour is incremented by a fraction of b_{small}. This is shown in the scheme of Figure 6. Given a small cell, the fraction of b_{small} which is transferred to each regular neighbour is proportional to the fluid surface shared with that neighbor. Once the transfer is done, the independent term of Poisson equation for the small cells becomes zero. The pressure equation is solved and the mass at the faces can be computed using equation 17.

The above technique conserves mass regionally but not locally, as is explained in [46]. The regional conservation ensures the global mass conservation.

2.4. Energy equation

The time integration of the energy equation is performed explicitly with a self-adaptive strategy applying the following equations in matrix form:
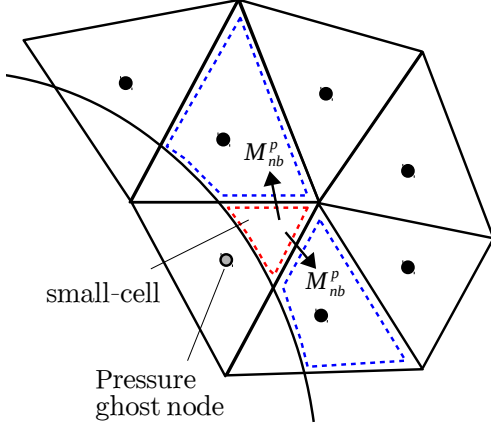
9

Figure 6: Schematic of virtual cell merging technique. Independent term of pressure Poisson equation is transferred to non-small neighbours cells

$$\Omega \frac{\sigma_1 T^{n+1} - (\sigma_2 T^n + \sigma_3 T^{n-1})}{\Delta t} \quad = \quad \alpha_0 H_T(T^n) + \alpha_1 H_T(T^{n-1}) + s_{IB}^{n+1} \tag{18}$$

$$H_T(T) \quad = \quad -C\left(u\right)T + \frac{\lambda}{\rho c_P} DT + S(T) \tag{19}$$

where Ω is a diagonal matrix with the sizes of control volume and H_T is a spatial operator containing the convective and diffusive operators ($C\left(u\right)$ and D respectively), and an energy source term S used in this work to consider radiative exchange between surfaces. The coefficients α_i and σ_i correspond to the $\kappa 1L2$ method used in this work.

For the conjugate problem, the numerical stencils used to discretize the equation (18) are adapted to consider the presence of a solid. The term $(\rho c_P)_k$ for each cell k is computed by using the volume fractions of fluid and solid calculated for the Poisson equation modifications:

$$(\rho c_P)_k = \frac{(\rho c_P)^F V_k^F + (\rho c_P)^S V_k^S}{V_k} \tag{20}$$

In the following sections, the convection, diffusion and source terms are explained.

2.4.1. Diffusion term

The discretization of the diffusion term using the finite-volume method for a particular control volume k is:

$$\left(\frac{\lambda}{\rho c_P} DT\right)_k = \frac{1}{(\rho c_P)_k} \sum_{f \epsilon \mathcal{F}(k)} \lambda_f (\nabla T)_f \cdot \vec{n}_f A_f \tag{21}$$

The direct gradient evaluation is used to estimate the temperature gradient in the cell face (equation (22)). In faces where the cells belong to different materials, the harmonic mean is used to compute λ_f as is
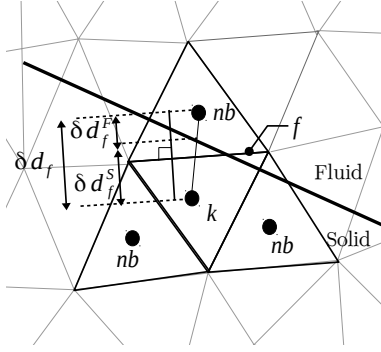
Figure 7: Geometric parameters of the evaluation of the diffusion term on cells near the interface.

expressed in equation (23). The distances δd_f^S and δd_f^F (see Fig. 7) represent the normal-projected distance from the nodes to the immersed boundary, projected with the face normal.

$$(\nabla T)_f \cdot \vec{n}_f \;=\; \frac{T_{nb} - T_k}{\delta d_f} \tag{22}$$

$$\lambda_f \;=\; \delta d_f \left(\frac{\delta d_f^F}{\lambda^F} + \frac{\delta d_f^S}{\lambda^S} \right)^{-1} \tag{23}$$

2.4.2. Convection term

The finite-volume discretization of the convection term for a particular control volume k is:

$$(C\,(u)\,T)_k = \frac{1}{(\rho c_P)_k} \sum_{f \epsilon \mathcal{F}(k)} (c_P)^F \dot{m}_f T_f \tag{24}$$

where the mass flow $\dot{m}_f$ was computed during the resolution of momentum and continuity equations. The temperature at face T_f is computed using the classical second order skew-symmetric scheme in regular faces, and a reconstruction procedure is employed to estimate the temperature T_f at the centroid of cut faces by the body.

To explain the reconstruction procedure, lets consider the cut face of Figure 8, which is indicated with a red rectangle. The centroid of the cut face, where the temperature must be estimated, is marked with a red point ($\vec{X}_{fC}^F$). For that point, during the pseudo mass reconstruction, three neighbours (two in case of 2D geometry) in the fluid region were selected (blue points in the Figure), and their corresponding coefficients a_i were computed using the procedure described in Section 2.2 for the velocity and temperature reconstruction at the forcing points. Normalizing these coefficients with equation (25), and employing equation (26), the temperature T_F at $\vec{X}_F$ can be estimated. The location $\vec{X}_F$ is defined by the intersection between the normal line to the immersed boundary passing through $\vec{X}_{fC}^F$ and the plane defined by the fluid neighbors used for the interpolation (see Fig. 8).

$$b_i \;=\; \frac{a_i}{\sum_i a_i} \tag{25}$$
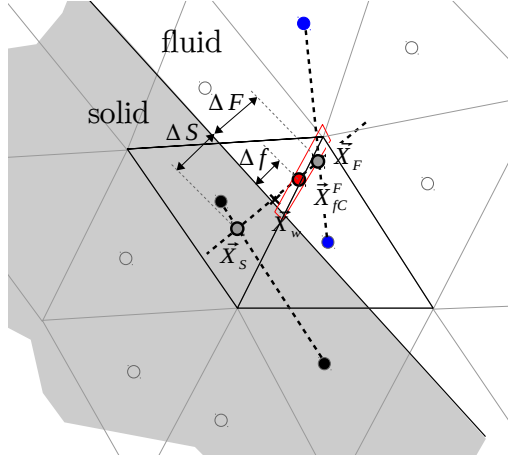
$$T_F \;=\; \sum_i b_i T_i \tag{26}$$

11

Figure 8: Geometric parameters of the evaluation of the convection term on cells near the interface.

Analogue to that, three neighbours (or two in 2D) from the solid region can be selected (black points in Figure 8). Coefficients are computed in order to estimate the temperature T_S of the auxiliary point $\vec{X}_S$. This point is defined by the intersection between the normal line to the immersed boundary passing through $\vec{X}_{fC}^F$ and the plane defined by the solid neighbors used for the interpolation (see Fig. 8).

After T_F and T_S are obtained, the temperature T_f is calculated. First, the temperature at the wall T_w is computed with equation (27), and finally T_f is calculated using (28):

$$T_w = \frac{T_S \frac{\lambda_S}{\Delta_S} + T_F \frac{\lambda_F}{\Delta_F}}{\frac{\lambda_S}{\Delta_S} + \frac{\lambda_F}{\Delta_F}} \tag{27}$$

$$T_f = T_w + \frac{\Delta_f}{\Delta_F}(T_F - T_w) \tag{28}$$

where ΔF, ΔS and Δf are the distance from the interface to $\vec{X}_F$, $\vec{X}_S$ and $\vec{X}_{fC}^F$ to the immersed boundary, respectively.

2.4.3. Radiative transfer equation

In order to consider the radiative exchange between surfaces, the source term $S(T)$ of equation (19) takes a non-zero value in the interior forcing points (see Fig. 2).

To calculate the term $S(T)$ used in equation 19, the net radiation problem [47] is solved at each time iteration. Two kinds of surfaces are involved in the problem: those from boundaries of the domain, referred to as "boundary surfaces", and (ii) those from the immersed bodies, referred to as "body surfaces". For both cases, surfaces were defined as a group of faces selected in the pre-process. The "boundary surfaces" are composed by boundary faces of the Eulerian mesh, and the "body surfaces" are composed by faces of the Lagrangian mesh (STL file). The number of surfaces depends on the nature of the problem. Therefore, the calculation of the radiative fluxes could range from enormously costly to nearly neglectable.

An example of the definition of surfaces is presented in Figure 9. In this example, six surfaces are defined, each colour corresponds to a different one. Four are of the type "boundary surfaces", and the other two are "body surfaces". For example, the brown "body surface" is composed by six elements of the Lagrangian mesh, and the red "boundary surface" has ten faces of the Eulerian mesh.

Once the surfaces are defined, assuming gray and diffuse surfaces, the net radiative heat flux per unit of
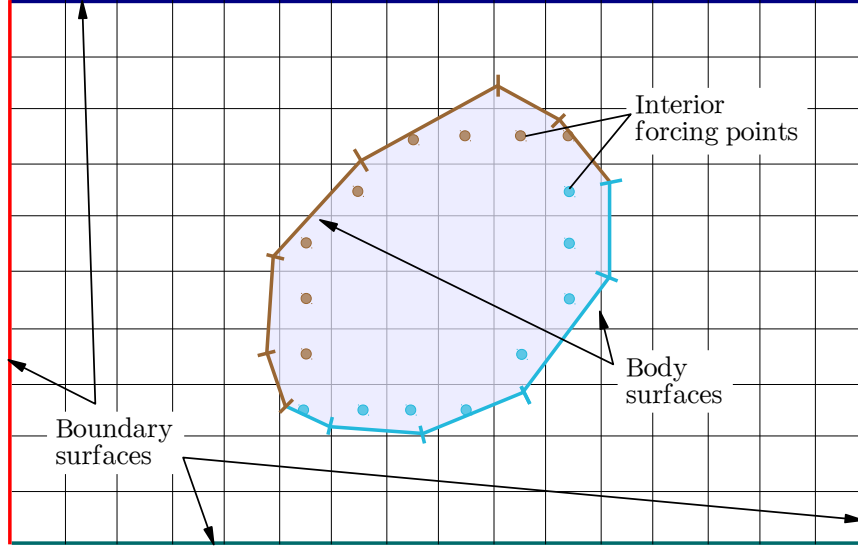
Figure 9: Representative domain and definition of "body surfaces" and "boundary surfaces". Each colour corresponds to a particular surface.

area for each surface i, $q_R(i)$, can be calculated by solving the net radiation system [47]:

$$\frac{q_R(i)}{\varepsilon_i} - \sum_{j=1}^{N} \left(\frac{1}{\varepsilon_j} - 1\right) F_{ij} q_R(j) = \sum_{j=1}^{N} F_{ij} \sigma \left(T_i^4 - T_j^4\right), i = 1, 2, ..., N \tag{29}$$

where A_i is the area of the surface i, N is the number of surfaces, $\sigma = 5.67 \times 10^{-8} W/m^2 K^4$ is the Stefan-Boltzmann constant, ε_i is the emissivity of surface i, and F_{ij} is the view factor between surfaces i and j, which is calculated using the ray-tracing method [48, 49]. The mean temperatures T_i are calculated at each time step for both "boundary surfaces" and "body surfaces". For the latter, the calculation was done via interpolation, using the information of the interior forcing points. The radiation system is solved by the GMRES [50] iterative solver, based on Krylov subspace projection methods.

Finally, the heat fluxes $q_R(i)$ are included in the time integration of the energy equation. At the "boundary surfaces" they are directly imposed as a boundary condition, while for the "body surfaces" the energy is included as a source term $S(T)_k$ in the interior forcing points, which is computed using equation 30.

$$S(T)_k = -q_R(i) A_p(k) f_G(i) \tag{30}$$

where the interior forcing point k belongs to the surface i. In the example of Figure 9, the interior forcing points which belong to a "body surface" are coloured with the same colour as the Lagrangian elements of that surface. $A_p(k)$ is the projected area of the cell in the body's interfaces, and $f_G(k)$ is a geometric corrector factor used to ensure the energy conservation (see below).

A_p is computed using:

$$A_p(k) = \sum_{f \in \mathcal{F}_F(k)} A_f \vec{n}_f \cdot \vec{n}_{IB} \tag{31}$$

13

where $\mathcal{F}_F(k)$ are the faces of the control volume k corresponding to a fluid neighbour (see Figure 10).
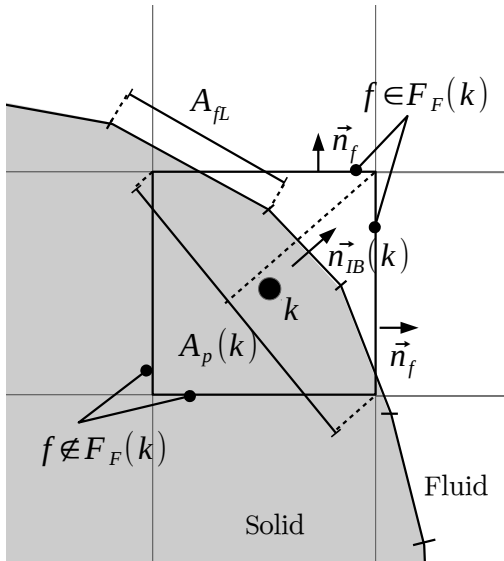

Figure 10: Geometric parameters of the evaluation of the radiative term on cells near the interface.

As the projected area A_p does not necessarily coincide with the real area of the Lagrangian mesh intersected by the cell, the geometric correction factor $f_G(i)$ must be introduced to conserve energy. This factor is computed for each "body surface" using the following equation:

$$f_G(i) = \frac{\sum_{f_L \epsilon i} A_{f_L}}{\sum_{k \epsilon i} A_p(k)} \tag{32}$$

where $f_L \epsilon i$ are the faces of the Lagrangian mesh which form the surface i, and A_{f_L} are their areas. $k \epsilon i$ are the interior forcing points for which it closest triangle of the Lagrangian mesh belongs to surface i.

3. Validation and verification of the method

To validate and verify the solver, three cases have been simulated. The first case is an accuracy study of the flow in concentric cylinders. The second case is selected in order to test the modification of the pressure-velocity decoupling procedure introduced, consisting of a flow in a infinitely long channel with thin baffles mounted periodically. Finally, Case 3 is a conjugate heat transfer problem taken from literature where radiation between surfaces must be taken into account.

The validation tests has been performed in an personal computer Intel(R) Core(TM) i5-4670 CPU @ 3.40GHz, engaging up to 4 CPU-cores.

3.1. Case 1. Concentric cylinder accuracy study

To study the accuracy of the method, the case of the flow between two concentric cylinders is considered. Figure 11a shows a scheme of the case, where two concentric rings are considered. The small ring is static and has an inner radius of $R_1 = 0.12m$ and an exterior radius of $R_2 = 0.2m$. The radius of the inner wall of the outer ring is $R_3 = 0.48m$, and is rotating with an angular velocity of $\Omega = 0.5 rad/s$. The tangential velocity of its inner wall is $u_\theta(R_3) = U_3 = 0.24m/s$. The analytic solution of the velocity for this problem is:

$$u_\theta(r) = \frac{R_3 R_2^2 U_3}{R_2^2 - R_3^2} \frac{1}{r} - \frac{R_3 U_3}{R_2^2 - R_3^2} r$$

$$u_r(r) = 0 \tag{33}$$

For the thermal problem, the heat conduction inside the small ring is computed in order to have a conjugate heat transfer problem. In the interior face of the small cylinder a constant heat flux is imposed, $\dot{Q}_1 = 15.08W$ (depth $b = 1m$), and a Dirichlet condition $T_3 = 300K$ is used at R_3. Moreover, the radiative exchange between the solids surfaces has been considered.

Once the steady state regime is reached, the temperature at the enclosure of the inner ring is uniform at some value T_1, and all the heat q_{IN} is conducted through the solid ring to the enclosure conformed by the two solids. The temperature of the exterior surface of the small ring is defined as T_2. The analytic solution of the energy equation is:

$$T(r) = \begin{cases} T_2 + \frac{T_1 - T_2}{ln\left(\frac{R_1}{R_2}\right)} ln\left(\frac{r}{R_2}\right) & R_1 \leq r \leq R_2 \\ T_3 + \frac{T_2 - T_3}{ln\left(\frac{R_2}{R_3}\right)} ln\left(\frac{r}{R_3}\right) & R_2 \leq r \leq R_3 \end{cases} \tag{34}$$

where T_1 and T_2 can be computed by solving the set of equations:

$$\dot{Q}_1 = \frac{2\pi b \lambda_S}{ln\left(\frac{R_2}{R_1}\right)}(T_1 - T_2) \tag{35}$$

$$\dot{Q}_1 = \frac{2\pi b \lambda_F}{ln\left(\frac{R_3}{R_2}\right)}(T_2 - T_3) + 2\pi R_2 b \varepsilon_2 \sigma(T_2^4 - T_3^4) \tag{36}$$

where $\sigma = 5.67 \times 10^{-8} W/m^2 K^4$ is the Stefan-Boltzmann constant, and ε_2 is the emissivity of the the surface R_2. Here, it is assumed that R_3 is black ($\varepsilon_3 = 1$).

Two configurations are considered, with and without radiative exchange:

Case 1A The radiative exchange is forced to be zero by defining $\varepsilon_2 = 0$. A value of $\lambda_F = 0.03W/mK$ was used for the conductivity of the fluid, and a value of $\lambda_S = 0.3W/mK$ for the solid. With these parameters, the analytical solution is $T_1 = 374.1K$ and $T_2 = 370K$.

Case 1B To consider radiative exchange, a positive value of $\varepsilon_2 = 0.0145$ is used for the emissivity of the surface R_2. The conductivities are the same as in case 1A. The analytical solution in this case is $T_1 = 346.8K$ and $T_2 = 342.7K$. With these parameters, the radiation heat accounts for 39% of the total heat exchanged.

These cases allow to evaluate the quality of the reconstruction of the boundary for momentum and energy equations with the approach presented in this work, in non-body conformal immersed boundary, with curved walls in cartesian meshes. The domain used is a square of side $L = 1m$ concentric to the cylinders. Three different meshes were used with sizes of: (a) 20×20, (b) 50×50 and (c) 100×100. The mesh (b) together with the solids are shown in Figure 11a. To simulate these cases one CPU-core was used, to reach the steady 50 minutes of real-time simulation was needed for case 1B using the finest mesh. The computed temperature
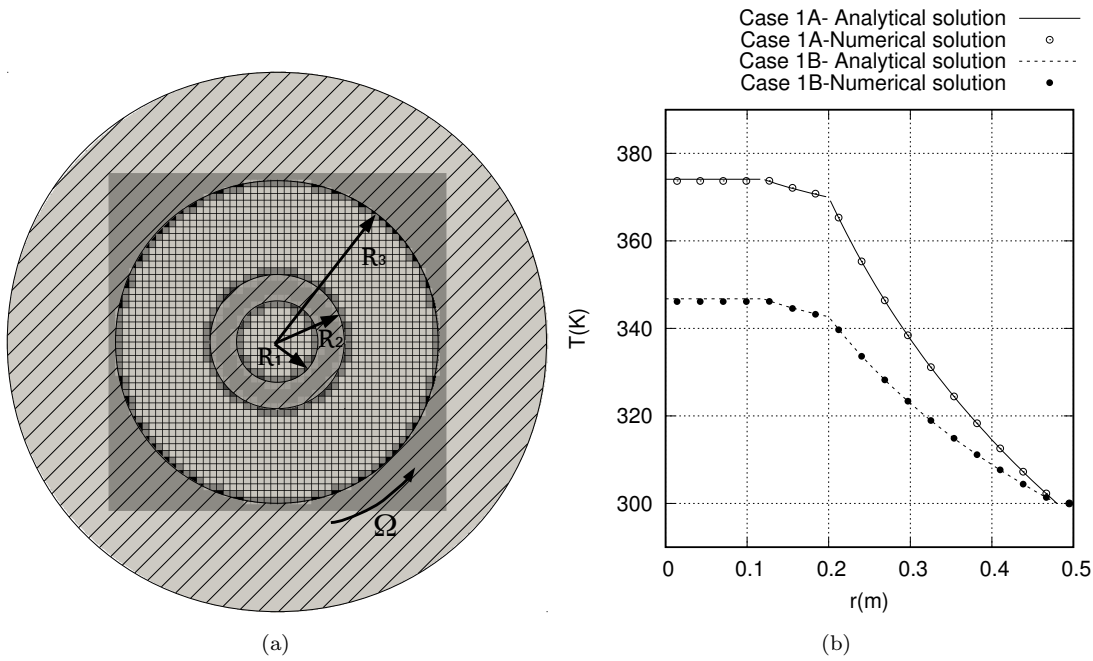
15

Figure 11: (a) Scheme of the case and 50×50 mesh (b), exterior forcing point in gray and interior forcing points in black. (b) Temperature distribution for cases 1A (no radiation) and 1B (with radiation).

profile using mesh (b) in cases 1A and 1B is compared to the analytic solution in Figure 11b. As can be seen, even with a relatively coarse mesh the solution is well reproduced.

The L_1 norm of the error is computed as:

$$L_1 = \frac{1}{N} \sum_{i=1}^{N} |\phi^t(i) - \phi^c(i)| \tag{37}$$

where the ϕ^t is the analytical solution and ϕ^c is the computed solution. The N nodes considered for each mesh are only the ones located in the fluid region. The L_1 norm of the error of the velocity is plotted as a function of the mesh resolution h, including lines representing dx and dx^2 in Figure 12a. As can be observed, the error increases proportional with dx^2, which illustrates the second-order of the momentum solver. Moreover, fitting the data with the function $a(dx)^n$, a value of $n = 2.013$ is computed.

The L_1 norm of the error of the temperature is plotted in Figure 12b for cases 1A and 1B. For configuration 1A, where radiative exchange is not considered, second order of accuracy is observed, more precisely $n = 1.979$. Therefore, the boundaries are represented within the accuracy of the numerical scheme. For the configuration 1B, where the radiative exchange is considered, less than a first order is observed with $n = 0.835$. This is probably due to the fact that the radiative heat depends on the fourth power of the temperature.

3.2. Case 2. Baffled channel

This second case corresponds to a flow in a infinitely long channel with baffles mounted periodically in the x-direction. A computational domain that contains only one period is simulated. Periodic boundary conditions are set at the inlet and outlet sections, and a pressure gradient is added in the x-direction. The domain configuration is shown in Figure 13. The geometrical parameters were chosen to match the conditions
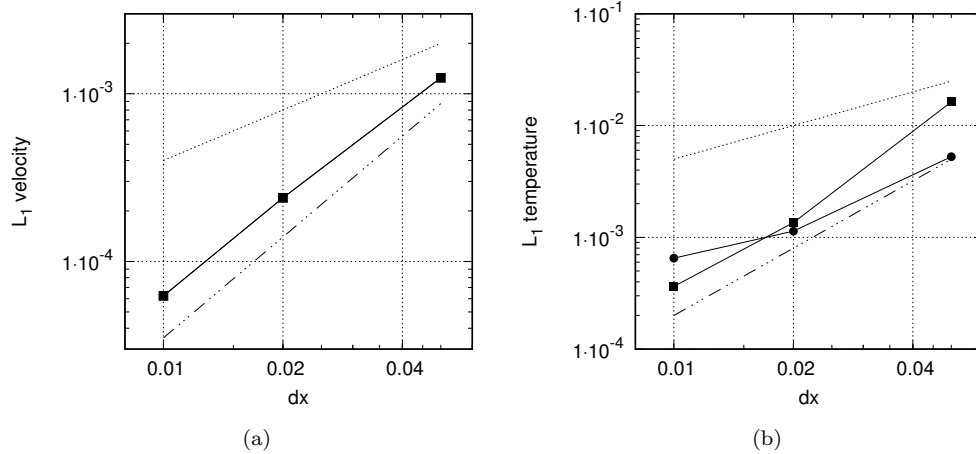
16

Figure 12: L_1 norm of the error vs. mesh resolution (dx): (a) Velocity (squares for case 1A and 1B); (b) temperature (circles for case 1A and squares for case 1B). Linear and second-order variations are indicated by dotted and dash-dotted lines, respectively.

of the experiment carried out by Roberts [51]. The distance between baffles is $L = 1.4$, the channel height is $H = 1$, and the baffle height is $B = 0.25$ (non-dimensional distances). A cartesian mesh with size of 210×150 was used. The baffles were modeled as immersed boundaries as is shown in Figure 14, the location of the baffles were defined in order to ensure a non-conformal approach.
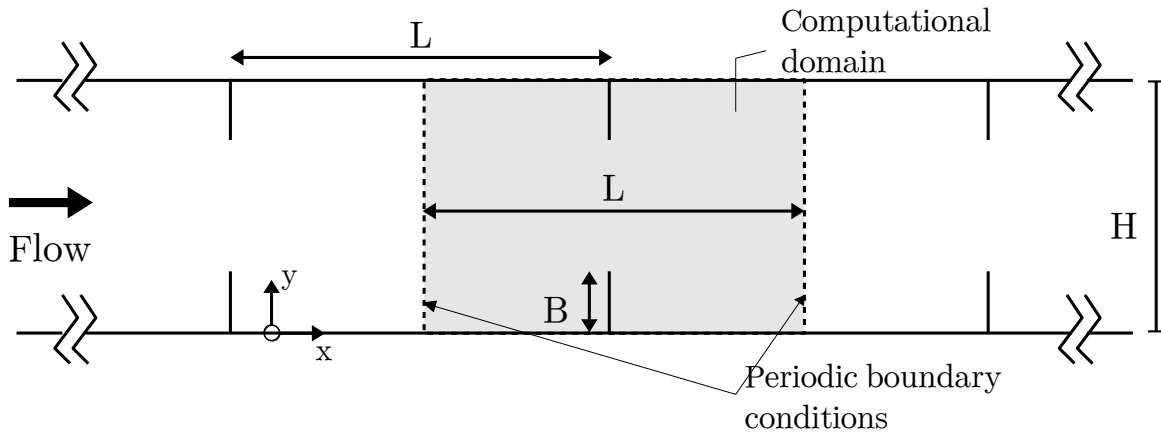
Figure 13: Geometry of a baffled channel. Computational domain.

The Reynolds number defined as $Re = U_m H / \nu$ was set to $Re = 60$, were U_m is the bulk velocity. Roberts [51] has also performed a numerical simulation of this case, using an accurate body-conformal approach obtaining excellent agreement with the experiment. The solution of this case is a two dimensional flow, symmetric in the y-direction, laminar and stable. The stream-lines obtained in the present work with two different approaches are compared with the reference solution computed by Roberts [51] in Figure 15. The red streamlines correspond to the solution obtained when the Poisson equation is not modified, and the blue streamlines to the solution computed with the modified Poisson equation. Due to the high pressure gradient between the sides of the baffles, unrealistic results are obtained when the immersed boundary condition is not explicitly imposed to the pressure field. In that case, the vortex located upstream the baffle is not formed,
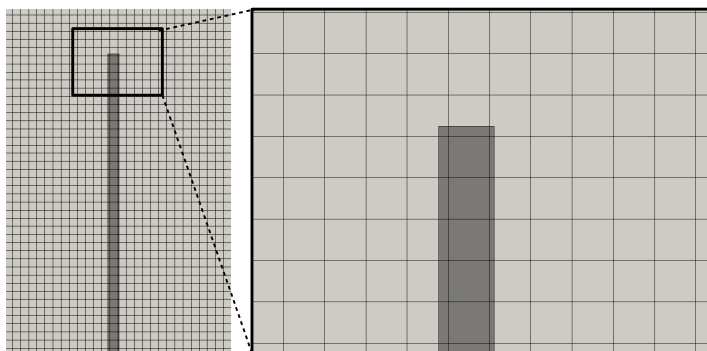
Figure 14: Mesh and baffle representation.

a mass passing through the body is observed, and the vortex located downstream the baffles is displaced forward in the direction of the mean flow. By using the new approach, these errors are avoided very well, the mass passing through the bodies is zero, and the streamlines matches the reference solution.
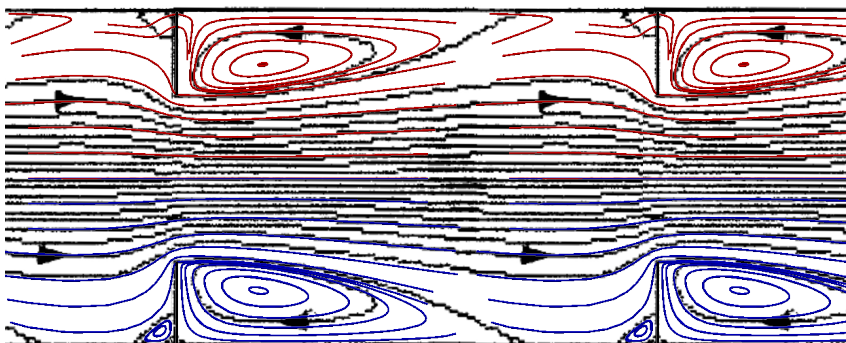

Figure 15: velocity streamlines of the flow in a baffled channel. Black: reference solution in [51]; Red: present simulation without Poisson modification; Blue: present simulation with Poisson modification.

In order to quantify the mass flux passing through the immersed boundaries two more cases, varying the Reynolds number, were simulated. The mass flux was computed using the following expressions:

$$M_T = \sum_{f \epsilon \mathcal{F}(x_b)} \dot{m}_f \tag{38}$$

$$M_B = \sum_{f \epsilon \mathcal{F}(b)} \dot{m}_f \tag{39}$$

where $\mathcal{F}(x_b)$ is the group of vertical faces located at the same x-coordinate than the baffles and $\mathcal{F}(b)$ are the faces of $\mathcal{F}(x_b)$ with it centroid inside a baffle. Then, M_T represents the total mass flux flowing at the channel, and M_B is only the non-physical mass flux that pass through the baffles. Using the new model, the mass passing through the baffles is strictly zero. However, when non boundary condition is imposed to the pressure equation, the mass passing through the baffles goes from 0.7% to 0.9% of the total mass flux at the channel. The results are summarized in Table 1.

To simulate these cases one CPU-core was used, to reach the steady state 3.2 hours of real-time simulation was needed.

18

	Modified Poisson	Non-modified Poisson
Re	M_B/M_T	M_B/M_T
45	0	0.00702
60	0	0.00788
85	0	0.00888

Table 1: Mass passing through the baffles using the modified and non-modified Poisson equation.

3.3. Case 3. 2D air-filled cavity with internal heat source

A surface thermal radiation and conjugate heat transfer case presented by Martyushev and Sheremet [4] was employed as the last verification case of this work. It consists of a square enclosure with heat-conducting solid walls of finite thickness. At the bottom, in contact with the fluid, a square heat source is located which maintains its superficial temperature at T_h. The exterior vertical walls lose heat by convection with an external fluid at temperature T_e and a convection coefficient h. The bottom surface is adiabatic, and the top surface is maintained at a constant temperature T_e. The configuration is schematically shown in Figure 16. The side of the internal square cavity is L, the thickness of the walls is $l = 0.2L$, and the side of the heat source is $d = 0.2L$.
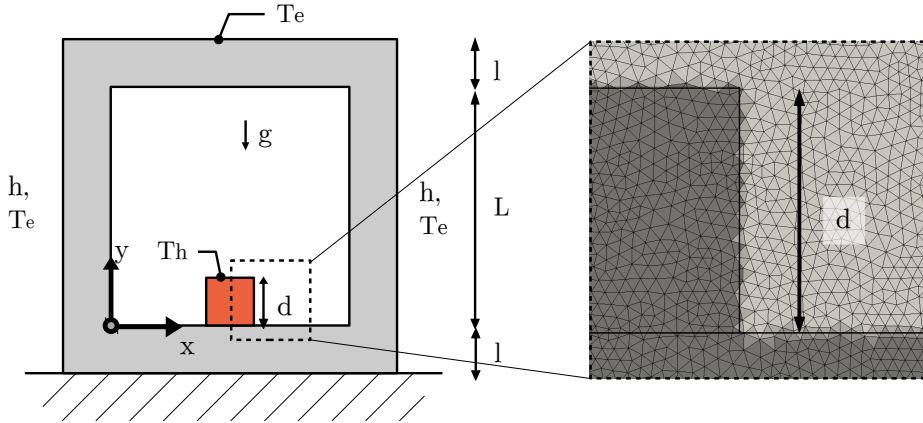

Figure 16: Scheme of square cavity with internal heat source and conducting walls (right); Mesh near the heat source (left).

Due to the simplicity of the geometry a structured mesh can be used. However, in this work an unstructured mesh composed by triangles was employed, to have a non-body conformal mesh in the solid-fluid interfaces. This can be observed in Figure 16, where details of the mesh in the vicinity of the heat source is shown. In this manner, the methodology of the boundary reconstruction can be better tested in this case. The size of the triangles is approximately uniform in the whole domain with $h/L \sim 0.01$, which means a total of 38436 cells.

Two solid bodies were included: one for the heat source and the other for the conducting walls, as can be seen in Figure 17. Note that despite the case is 2D, the solid geometry is fully 3D, which allows a more challenging test. The present methodology was implemented in TermoFluids [41] for generic 3D problems. However, imposing null derivatives for velocities and temperature at the boundaries in the z-direction give a 2D solution.

For the radiative equation, the internal walls were divided into 39 surfaces. Only one surface is used for
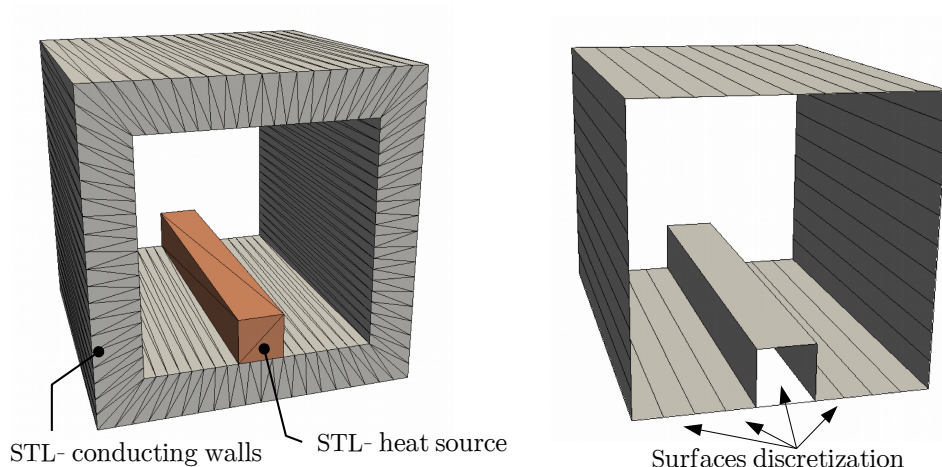
Figure 17: Picture of the STL files used to represent the immersed boundaries and discretization of the body surfaces for the radiation problem.
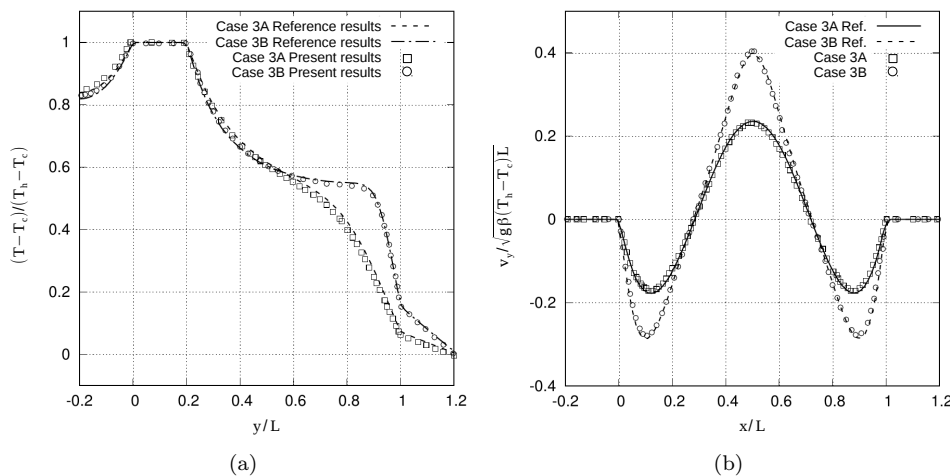

Figure 18: (a) Temperature distribution at the center line $x/L = 0.5$, and (b) vertical velocity distribution at the central line $y/L = 0.5$. Lines: reference results in [4]. Points: present results.

the heat source because it has uniform temperature. The remaining 38 were defined for the internal walls, as shown in Figure 17. The view factors were computed in the preprocess by the ray-tracing method.

To completely define the case, the following non-dimensional numbers were specified: Planck $Pl = \lambda_{fluid}(T_h - T_e)/(\sigma T_h^4 L)$, Biot $Bi = hL/\lambda_{solid}$, Raiyleigh $Ra = g\beta(T_{max} - T_{min})L^3/\nu\alpha_{fluid}$, Prandtl $Pr = \nu/\alpha$, the surface emissivities ε, and the ratio $K = \lambda_{solid}/\lambda_{fluid}$, where β is the coefficient of volumetric thermal expansion, ν is the kinematic viscosity and α is the thermal diffusivity of the fluid.

Two cases were simulated to match the conditions presented in [4]:

Case 3A $Ra = 10^4$ and $Pl = 0.19$.

Case 3B $Ra = 10^5$ and $Pl = 0.0877$.

For both cases $Bi = 2$, $K = 7$, $Pr = 0.7$ and the emissivity of all the internal surfaces was set at $\varepsilon = 0.6$.
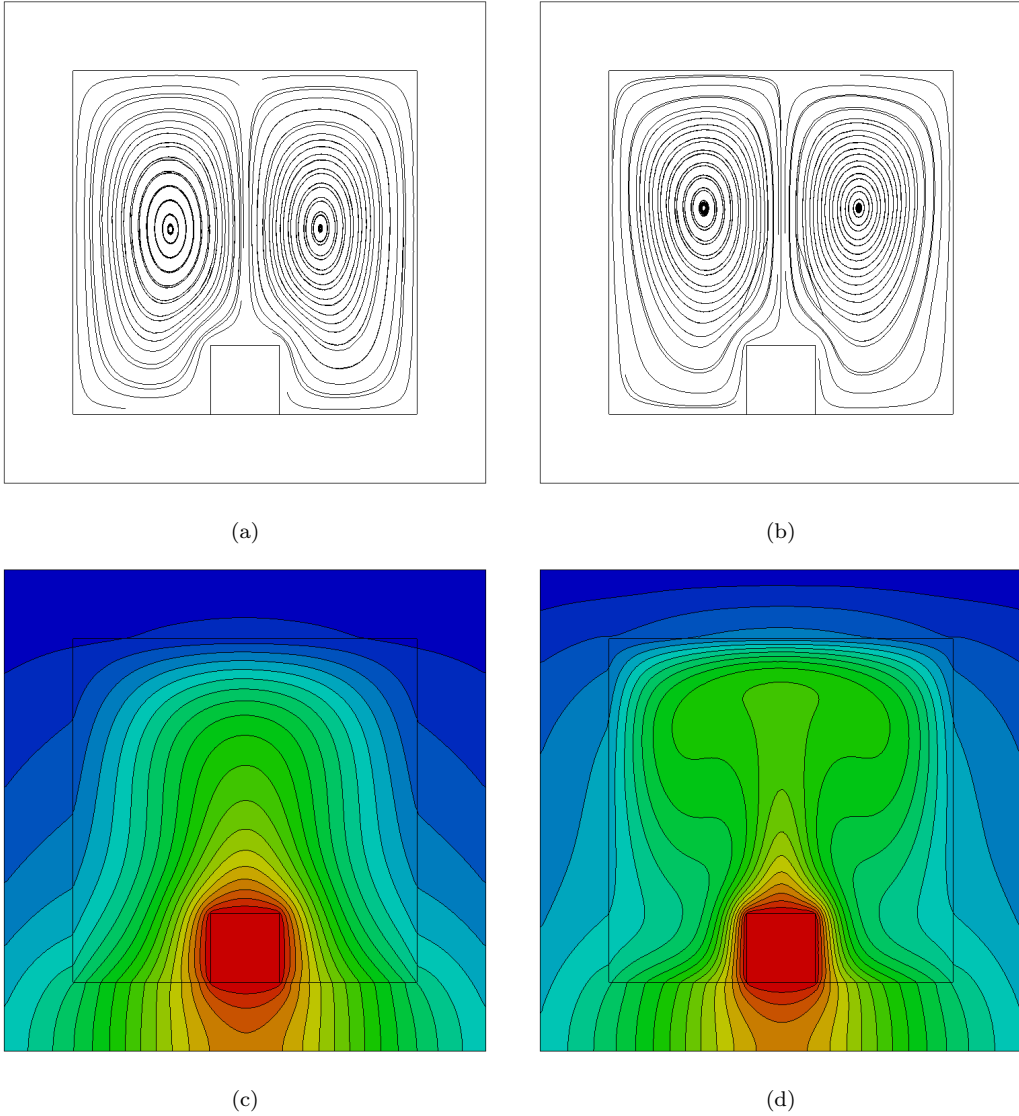
Figure 19: Streamlines for (a) case 3A ($Ra = 10^4$, $Pl = 0.19$), and (b) case 4B ($Ra = 10^5$, $Pl = 0.0877$). Temperature contour plots for (c) case 3A and (d) case 4B.

For these conditions the flow reaches a stationary laminar regime. To simulate these cases four CPU-core were used, to reach the steady state 6 hours and 7 hours of real-time simulation was needed for cases 3A and 3B respectively.

Temperature and vertical velocity distributions along the lines $x/L = 0.5$ and $y/L = 0.5$ respectively, are presented together with the solution obtained in [4] in Figure 18. Streamlines and isotherms for each case are shown in Figure 19. Two symmetric convective cells are formed into the cavity and a thermal plume in the central part. For the case with the bigger Ra (3B), the cores of the convective cells are located in an upper position and the thermal plume is more intense. These results are in very good agreement with those presented in [4].

To solve this problem, Martyushev and Sheremet [4] employed a body-conformal approach discretizing

the governing equations in two separate computational domains, one for the fluid region and the other one for the solid walls. They previously verified their solver by simulating benchmark cases. In those cases the convection was combined with conduction or radiation. In the present work, we have been able to reproduce the results obtained in [4] accurately using a non-body conformal approach, which allows to approach cases with very complex geometries in a relatively simple way.

4. Application to a car component

In the framework of a collaboration project with FICOSA, the methods presented in this work were used to study the thermal behaviour of a Smart Antenna Module (SAM, Figure 20). A SAM is a car component which combines antenna elements and radio receivers in one package, including a printed circuit board (PCB) with the electronics needed for a number of applications, i.e. GPS, WiFi, emergency calls, etc.

A correct design which allows to dissipate the generated heat at the SAM, maintaining the temperature of the components under the critical values, prolongs its useful life and increases its reliability. The aim of the collaboration was to study the thermal behaviour of the original design for a specific working configuration, and improve it with the minimum structural changes possible.
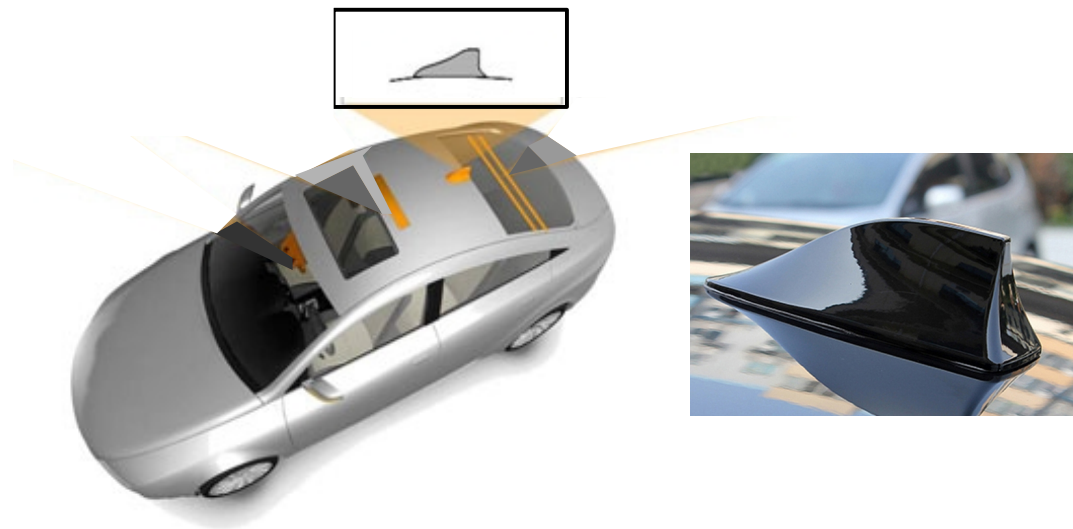

Figure 20: Exterior of a Smart Antenna Module.

By using CFD to simulate this problem, it is possible to obtain detailed and reliable data, avoiding huge geometric simplifications and assumptions. One strategy to perform the simulation is to have one mesh for each solid component and one mesh for each air enclosure. These are treated as separate problems, but connected by boundary conditions if they are in touch. For this particular problem, with a big number of components with complex geometries, the meshing process could make the project unfeasible. These meshes must have a minimum of good quality, and the generation of each one is an extremely demanding task. This is even more critical if the possibility of comparing different geometries is considered.

However, by using the IBM, the meshing process is highly simplified. Only one volumetric mesh is needed, and the components can be represented by superficial meshes (STL) with no quality restrictions, obtained directly from the geometry provided by the company. In this project the volumetric mesh is conformed by hexahedrals and is locally refined depending on the components geometry, as it will be explained later.

In the following sections the problem is analysed. In section 4.1, the boundary conditions and the geometry and properties of the component of the SAM are described. Some numerical aspects are also explained. Finally, in Section 4.2 the results are presented for the original configuration and for the proposed improvements, comparing the different alternatives.

4.1. Problem description and numerical considerations
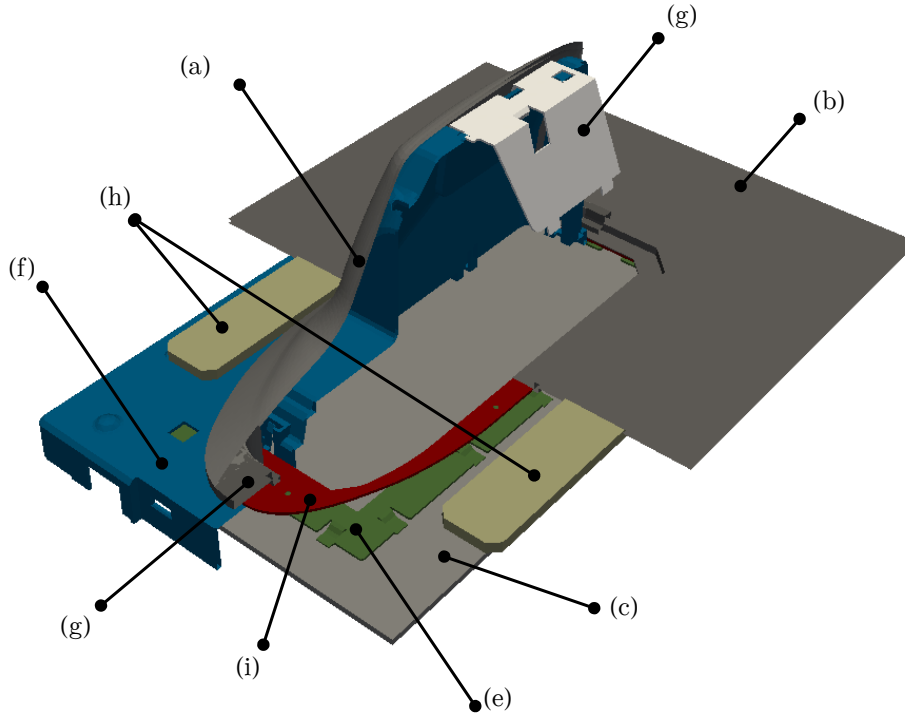
4.1.1. Geometry description

Figure 21: Solid parts included in the simulation. Picture taken using the STL files used to represent the interfaces in its locations. The letters detail the parts described in Table 2.

The pieces that form the SAM are shown assembled in Figure 21. The same pieces are shown apart in Figure 22. In both cases the pictures are taken from the surface meshes used in the simulation (STL files). These meshes are generated directly from the geometry provided by the company, except for the PCB in which some chips are not taken into account. The object (a) in Figure 22 is called Shark Cover because of its resemblance to a shark fin. It is designed to embellish the exterior of the SAM and to minimize the drag contribution. Object (b) is a section of the roof of the car. The PCB with the most important chips is the object (c), and the objects (d) and (e) are some metallic pieces which are in contact with the PCB. The object (f) is a plastic shell which contains all the electronics inside. Objects (g), (h) and (i) are structural parts needed to join all the other mentioned parts in a compact form. The material, properties and the number of triangles used in its corresponding STL files are given for each object in Table 2.
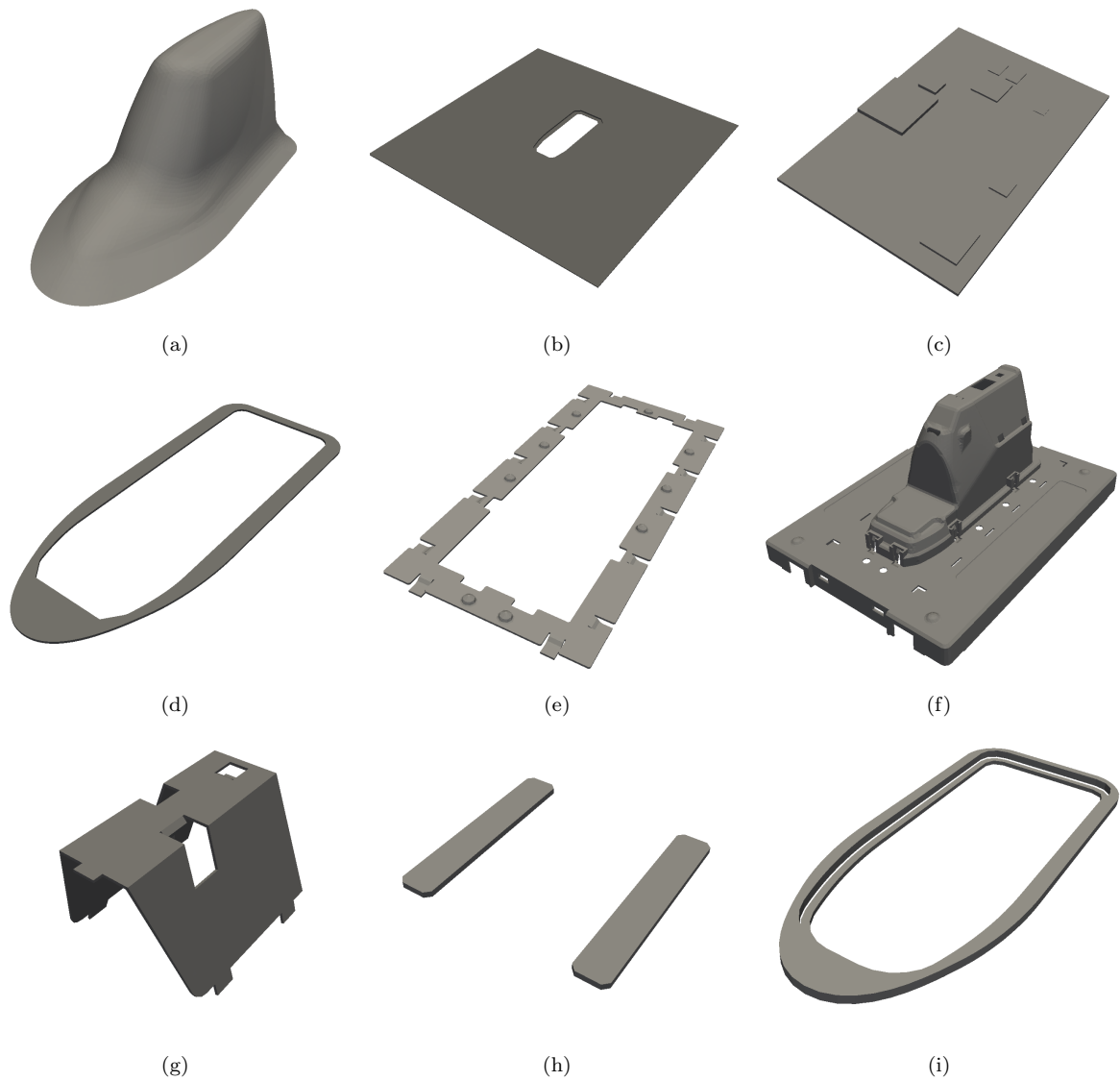
Figure 22: Single solid parts included in the simulation. Picture taken from the STL files used to represent the interfaces. The letters detail the parts described in Table 2. @2017 Advanced Automotive Antennas S.L All rights reserved patent EP 3174157 et alt. [52]

4.1.2. Boundary conditions

The boundaries of the SAM are shown in Figure 23: at the top, the shark cover is in contact with the external air and exposed to the sun radiation, and at the bottom, the structural box is in contact with the internal air of the car cabin.

Boundary conditions imposed are the heat losses calculated as a function of the wall temperature. For the case of the shark cover, the heat losses per unit area $\dot{q}_{Shark}$ are directly the convective and radiative ones:

$$\dot{q}_{Shark} = h_{ext}(T_S - T_{ext}) + \varepsilon_S \sigma (T_S^4 - T_{SKY}^4) - \alpha_S G_S cos\varphi \tag{40}$$

Object	Material	λ (W/mK)	ρc_P (kJ/m^3K)	ε	N^o triangles in STL
(a) Shark Cover	Plastic	0.20	1513	0.8	34026
(b) Roof	Steel	53.0	3611	0.8	1568
(c) PCB	-	34.0	2660	0.8	192
(d) Metallic Ring	Steel	53.0	3611	0.8	10968
(e) Contact Piece	Steel	53.0	3611	0.8	4658
(f) Shell	Plastic	0.25	1300	0.8	34699
(g) Structural part 1	Plastic	0.20	1300	0.8	2597
(h) Structural part 2	Plastic	0.20	1300	0.8	1224
(i) Structural part 3	Plastic	0.20	1300	0.8	1570

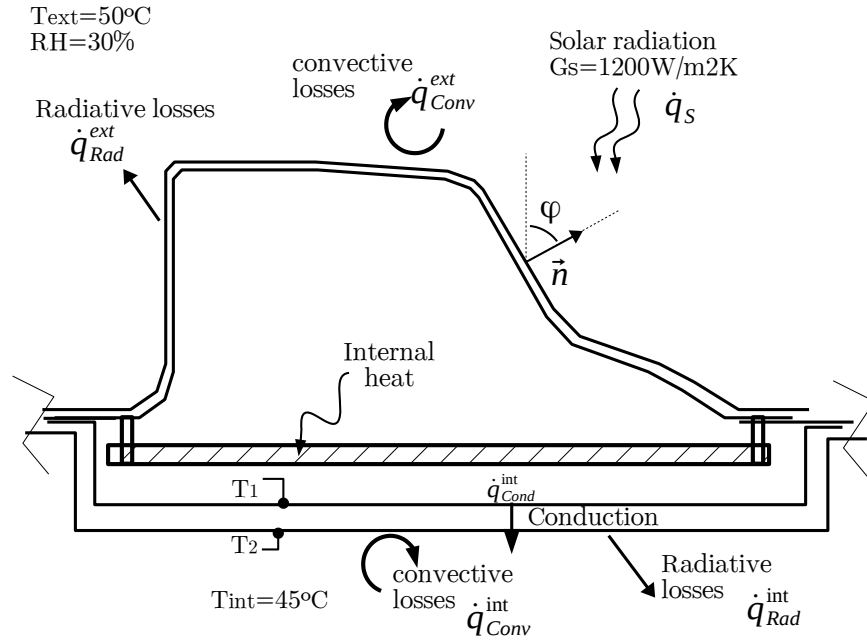Table 2: Physical properties of the solid parts and number of triangles used in the STL files.

Figure 23: Scheme of the problem and boundary conditions.

where T_S is the local temperature of the shark cover, T_{ext} is the temperature of the external air, h_{ext} is the external heat transfer convection coefficient, ε_S is the emissivity of the shark cover, T_{SKY} is the sky temperature, G_S is the solar radiance, α_S is the absorptivity of the external surfaces for short wave length and φ is the angle of the normal vector to the surface and the solar radiation direction (see Figure 23). The aim of the design is for the SAM to be able to function under extreme conditions, i. e. in a tropical climate at noon on a clear day. To represent these conditions, the air outside has a temperature of $T_{ext} = 50^oC$, and a relative humidity of $HR = 30\%$, which means a dew point temperature of $T_{dp} = 28^oC$. The solar radiance was set to $G_S = 1200W/m^2$, and the absorptivity $\alpha_S = 1$.

Using the correlation of Berdahl et. al. [53, 54] presented in equation (41), the sky temperature T_{SKY} is computed. In this correlation, the T_{dp} must be expressed in Celsius degrees, T_{ext} must be expressed in

Kelvin and t is the sun time in hours ($t = 0$ in this case). In this way a value of $T_{SKY} = 320K$ is obtained.

$$T_{SKY} = T_{ext} \left[\left(0.711 + 0.56(T_{dp}/100) + 0.73(T_{dp}/100)^2\right)^{1/4} + 0.013cos\left(\frac{2\pi t}{24}\right) \right] \tag{41}$$

To calculate the convection coefficient, the correlation for a vertical plate of Churchill et al. [55] was used, see equation 42. To take into account the inclination of the surface, the Rayleigh number was calculated replacing g by $gcos\theta$, where θ is the angle between the surface and the vertical vector, using a representative value of $\theta = 28^o$:

$$h_{ext} = \left(\frac{\lambda_{air}}{L}\right) 0.68 + 0.67Ra_L^{1/4} \left[1 + \left(\frac{0.492}{Pr}\right)^{9/16}\right]^{-4/9} \tag{42}$$

At the bottom, the box containing the electronic is isolated by a carpet. To calculate the heat losses per square meter through the carpet $\dot{q}_C$, the following equation is solved:

$$\dot{q}_{Cond}^{int} = \frac{\lambda_C}{e_C}(T_1 - T_2) = \varepsilon_C\sigma(T_2^4 - T_{int}^4) + h_{int}(T_2 - T_{int}) \tag{43}$$

where λ_C, e_c and ε_C are the conductivity, width and emissivity of the carpet, respectively, T_1 is the value of the temperature at the boundary of the computational domain, T_2 is the temperature of the carpet in contact with the internal air and T_{int} is the temperature of the internal air, and also of the internal surfaces. The coefficient h_{int} was computed using the correlation for a horizontal plate facing down from Fishenden et al. [56] of equation (44):

$$h_{int} = \left(\frac{\lambda_{air}}{L}\right) 0.25Ra_L^{1/4} \tag{44}$$

4.1.3. Internal heat sources

With the chips of the PCB working together in maximum power, a total heat of $\dot{Q}_I = 22.5W$ is generated. However, under the extreme conditions described above, the requirement for the SAM is to carry out only some specific operations. According to the information provided by the company, the generated heat by the electronics is set to $\dot{Q}_I = 10W$ in the simulation. The operative chips are indicated in Figure 24: (a) is the Telematic Module (TM), (b) is a microprocessor (μP) and (c) is a power management integrated circuit (PMIC) and they produce $\dot{Q}_{TM} = 3W$, $\dot{Q}_{\mu P} = 2W$ and $\dot{Q}_{PMIC} = 3W$, respectively. The remaining $2W$ of heat are distributed uniformly in the rest of the PCB.

4.1.4. Computational domain

The computational domain is shown schematically in Figure 25. It consists of two prismatic blocks which contain the SAM geometry. The mesh is composed by hexahedrals cells, and local mesh refinement is employed to minimize the number of elements. First, one mesh with uniform cell size of $dx = dy = dz = 2mm$ is generated, which has 0.3M control volumes. Based on this mesh, local refinement is applied in the cells with a distance to the objects shorter than $12.5mm$, splitting each in eight children cells [40]. This is done twice. Therefore, the cells in the interior and in the vicinity of the objects have a size of $dx = dy = dz = 0.5mm$. The
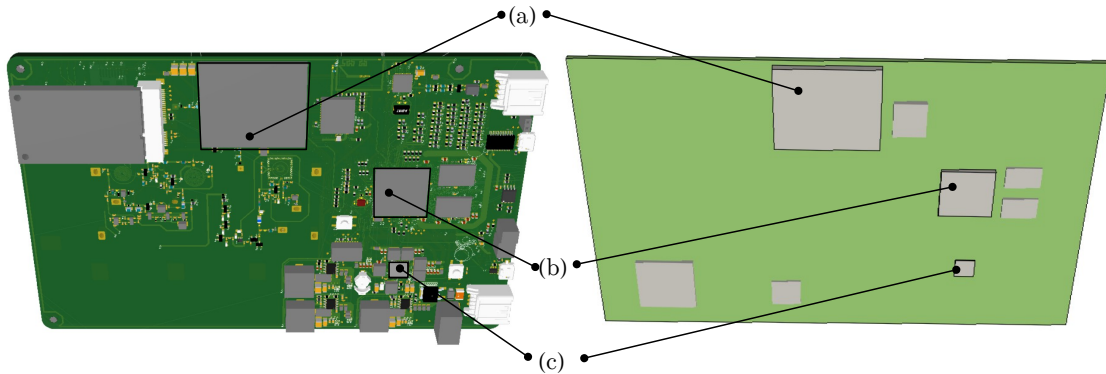
26

Figure 24: Real picture of the PCB and its simplification. The electronic chips operating in the simulations are indicated in the image: (a) Telematic Module (TM); (b) Microprocessor (μP); (c) Power management integrated circuit (PMIC).
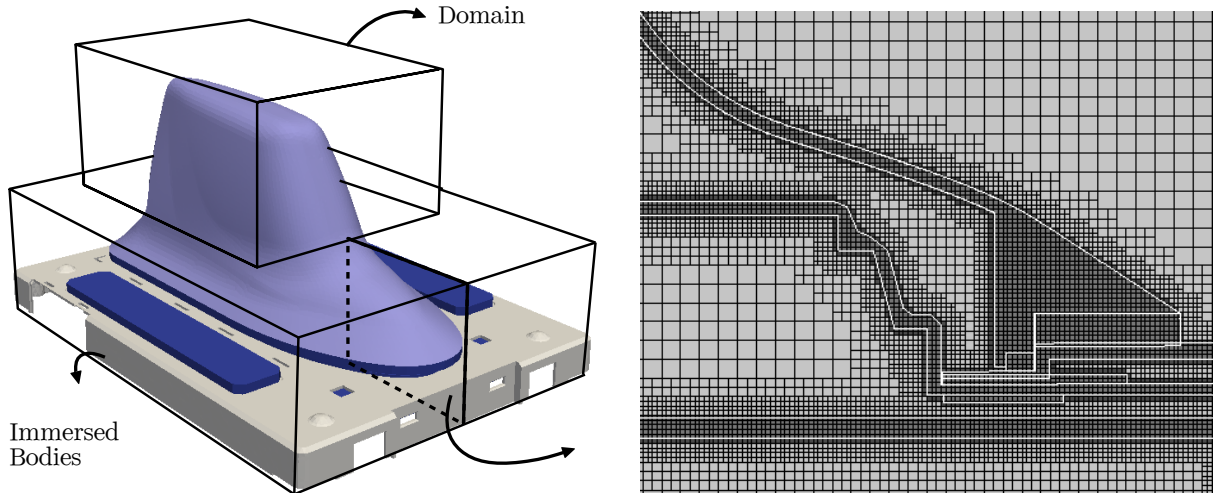

Figure 25: Computational domain and mesh near the front of the shark cover.

resulting mesh, including the objects mentioned previously, is conformed by 6.3M control volumes. However, different meshes are going to be used for different cases, in which dissipators will be included.

4.1.5. Net radiation problem

To calculate the radiative exchange between the internal surfaces, two enclosures shown in Figure 26 are considered: (a) the interior of the shell (Fig. 26a) and b) the space between the exterior surfaces of the shell and the interior surfaces of the shark cover (Fig. 26b. The view factors are calculated in the preprocess using the ray-tracing method.

4.1.6. Chip model

An electronic device reaches its maximum temperature at the silicon die within the package. This is known as Junction Temperature (T_J), and must be under a certain values to avoid damages. The thermal resistances
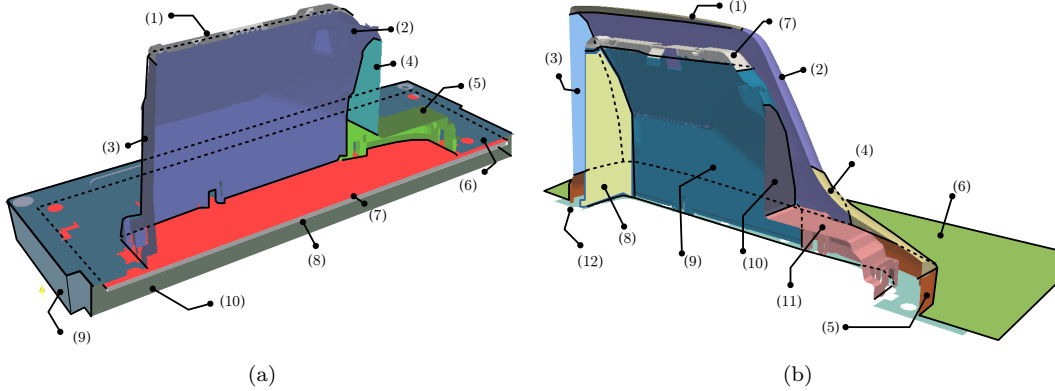
Figure 26: Surfaces definition for the net radiation problem: (a) exchange between PCB and internal surfaces of the shell and (b) exchange between external surfaces of the shell and internal surfaces of the shark cover and roof.

between the silicon die, and the adjacent parts of the electronic device are provided by manufacturers and must be included in the model to obtain an accurate estimation of the junction temperature of each device.

A scheme of the thermal model of a generic electronic device is shown in Figure 27. R_B and R_D are the thermal resistances from the silicon die to the PCB and to the ambient, respectively. In the case that a dissipator is installed, the patch thermal resistance R_P must be included. In the simulation, the cells inside a chip are set with high conductivity, and with an energy source term to imitate the silicon die. The temperature achieved in these cells will be considered as the T_J.

To include the chip model, the thermal conductivity at the faces, λ_f, is computed differently in the chip region. To do so, these faces are classified into three types (see Figure 27):

Type 1 The face has one cell at the chip and the other at the PCB. Then, interfacial thermal resistance between both cells is R_B.

Type 2 The face has one cell at the chip and the other in the ambient air. Then, interfacial thermal resistance between both cells is R_D.

Type 3 The face has one cell at the chip and the other at the aluminum dissipator. Then, interfacial thermal resistance between both cells is $R_D + R_P$.

The conductivity at these faces is calculated using the following equations:

$$Type\ 1: \quad \lambda_f = \left(\frac{d_J}{\lambda_J d} + \frac{d_{PCB}}{\lambda_{PCB} d} + \frac{R_B A_f^2}{A_B} \right)^{-1} \tag{45}$$

$$Type\ 2: \quad \lambda_f = \left(\frac{d_J}{\lambda_J d} + \frac{d_{air}}{\lambda_{air} d} + \frac{R_D A_f^2}{A_D} \right)^{-1} \tag{46}$$

$$Type\ 3: \quad \lambda_f = \left(\frac{d_J}{\lambda_J d} + \frac{d_d}{\lambda_d d} + \frac{(R_D + R_P) A_f^2}{A_D} \right)^{-1} \tag{47}$$

where λ_{air}, λ_d and λ_{PCB} are the thermal conductivity of the air, the dissipator and the PCB, respectively. d, d_{air}, d_{PCB} and d_d are distances indicated in Figure 27, A_f is the area of the face, A_B is the area of
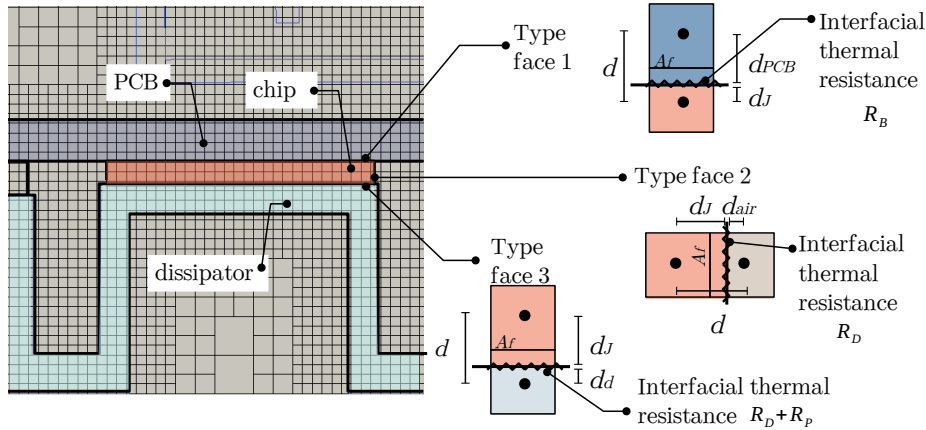
Figure 27: Thermal resistance model used for the electronic chips and implementation in the mesh faces.

the exterior of the chip in contact with the PCB or the air, and A_D is the area of the chip in contact with the aluminum dissipator. It must be noted that the contribution of the internal thermal resistances are computed as $R_B A_f^2 / A_B$ or $R_D A_f^2 / A_D$, as $R A_f / A_B$ and $R A_f / A_D$ are the fraction of thermal resistance for that particular face.

The values of R_D, R_B and R_P used for the chips were provided by the company and are the same for all the electronic devices. The areas of each device were computed directly from the geometry. This information is summarized in Table 3.

	R_D ($^o C/W$)	R_B ($^o C/W$)	R_P ($^o C/W$)	A_D (mm^2)	A_B (mm^2)
PMIC	2.90	0.60	2.60	76.8	64.0
μP	2.90	0.60	0.36	554	441
TM	2.90	0.60	1.23	162	126

Table 3: Values of thermal resistance and surface used for each electronic chip.

4.2. Results

The geometry described above corresponds to the original design, and is referred to in this work as Case 1. From the thermal point of view, it is easy to note that it is a low performance arrangement. The PCB is mostly in contact with air, and is thermally connected by metallic components only with the roof, which is the hottest element because of the solar radiation. The results for this case are summarized in the next section. As expected, the chips reach very high temperatures. Improved designs are tested. They consist of the installation of an aluminum dissipator in contact with the electronic chips, trying to dissipate the generated heat to the interior of the car. These configurations are referred to as Cases 2 to 4, and the details are presented in following sections.

Finally, the results obtained for the different cases are compared to one another. Moreover, the limits for the junction temperature are considered to analyze the designs and discuss possible improvements.

4.2.1. Case 1. Original Design

A temperature map of a vertical slide is shown in Figure 28. It is clear that for this configuration the hot body (PCB) is almost isolated from the cold parts (bottom surface and inclined sides of the shark cover). A convective cell is formed in the top enclosure, and at the bottom the air is stratified.
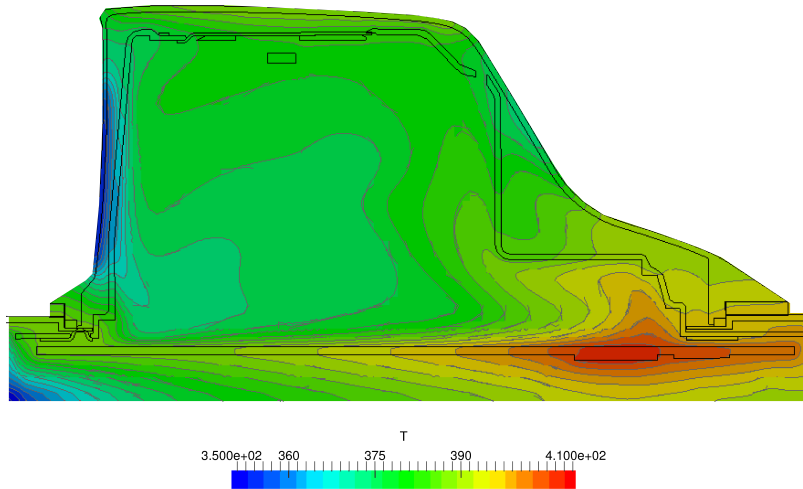

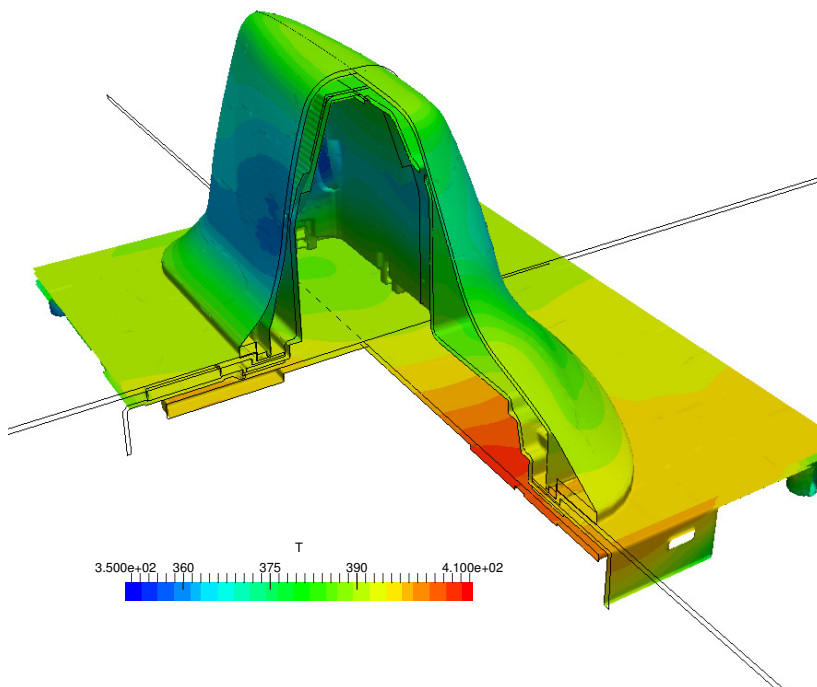Figure 28: Temperature contour plots of a side view in the middle of the domain for Case 1.

Figure 29: Temperature distribution in the surface of the solids parts for Case 1.

The global heat losses from the PCB can be divided into: radiative losses to the top $\dot{Q}_{Rad}^{Top}$, radiative losses through the bottom $\dot{Q}_{Rad}^{Bottom}$, convective losses to the top $\dot{Q}_{Conv}^{Top}$, convective losses through the bottom $\dot{Q}_{Conv}^{Bottom}$ and losses by conduction $\dot{Q}_{Cond}$. For this case, the computed values were $\dot{Q}_{Rad}^{Top} = 1.5W$, $\dot{Q}_{Rad}^{Bottom} = 4.5W$, $\dot{Q}_{Conv}^{Top} = 0.5W$, $\dot{Q}_{Conv}^{Bottom} = 2W$ and $\dot{Q}_{Cond} = 1.2W$. Note that the principal losses are through the bottom (65%), and comparing convective with radiative losses, the latter are the most important ones (63%). The conduction heat losses are small (12%), because of the small surface contact of solid parts with the PCB.

It could be surprising that the convective losses to the top enclosure are so small. However, it must be noted that the region where the air movement due to natural convection has an increase in the local Nusselt number; it is small compared to the total area of the PCB. Moreover, the remainder of the top surface of the PCB is close to a hot surface due to the solar radiation. A 3D view of the solid parts coloured with temperature is presented in Figure 29.

The junction temperatures of the TM, μP and PMIC for this configuration are $T_J^T = 136^oC$, $T_J^U = 144^oC$ and $T_J^P = 150^oC$, respectively. All of them are over the damage threshold, which is 130^oC.

4.2.2. Case 2. Built-in dissipator

T
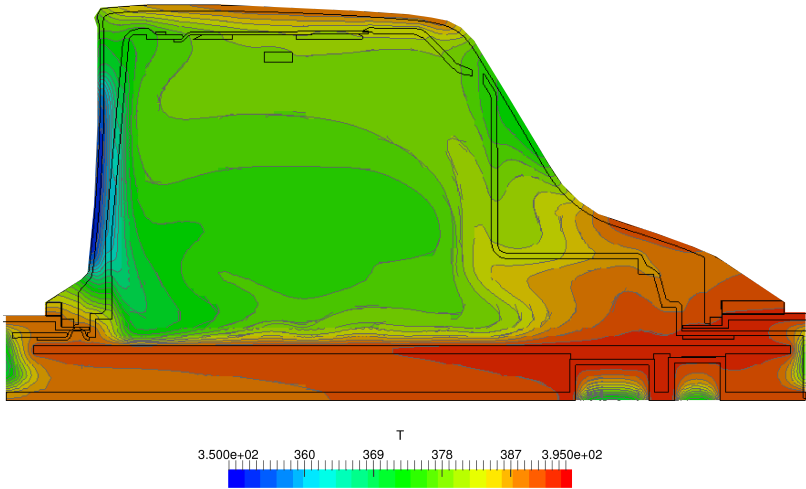3.500e+02   360   369   378   387   3.950e+02

Figure 30: Temperature contour plots of a side view in the middle of the domain for Case 2.

An aluminum dissipator is included for this case. It has a thickens of $d_{Al} = 1mm$, and it is in contact with the high-power chips and the bottom of the box. This can be observed in Figures 30 and 31. The junction temperatures are highly reduced with respect to the original design, with values of $T_J^T = 127^oC$, $T_J^U = 130^oC$ and $T_J^P = 131^oC$. However, they are still over the maximum possible value.

Thanks to the dissipator, the conduction losses are now predominant, with a value of $\dot{Q}_{Cond} = 7.6W$. Since the temperature of the PCB and the aluminum are quite similar, the losses by convection and radiation to the bottom are very small: $\dot{Q}_{Rad}^{Bottom} = 0.3W$ and $\dot{Q}_{Conv}^{Bottom} = 0.6W$. The reduction of the temperature of the PCB also decreases the heat losses to the top: $\dot{Q}_{Rad}^{Top} = 1.4W$ and $\dot{Q}_{Conv}^{Top} = 0.1W$.

4.2.3. Case 3. Built-in dissipator extended with aluminum sheet

In order to enhance the heat losses to the interior of the car, an extension to the base is included, as shown in Figure 32a. For this case, the extension consists of an aluminum sheet with a thickness of $d_{Al}^{ext} = 50\mu m$
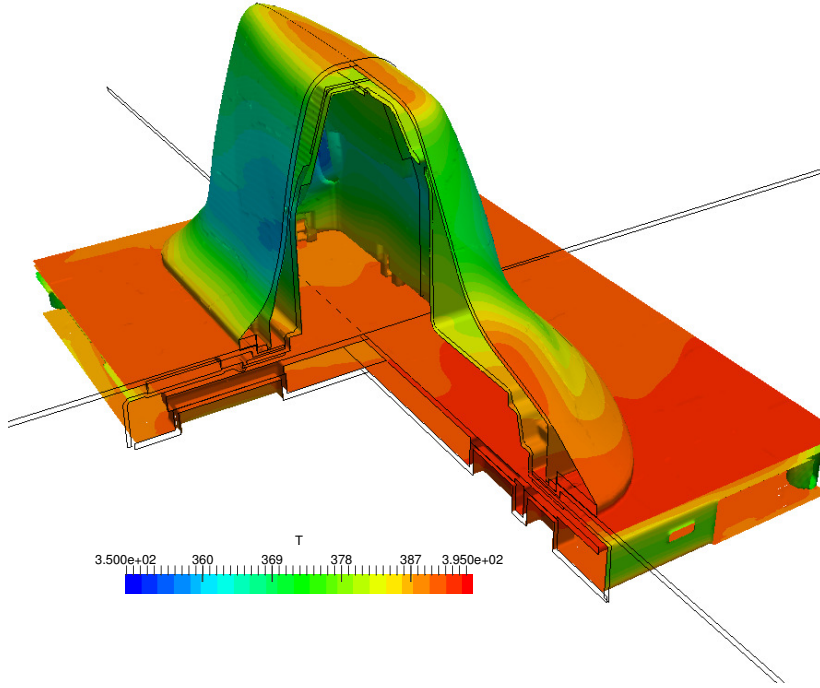
Figure 31: Temperature distribution in the surface of the solid parts for Case 2.

and dimensions of $L_X = 497mm$ and $L_Y = 496mm$. An insulator is placed between the base extension and the roof (see Figure 32b), to minimize the heat contribution from the top.
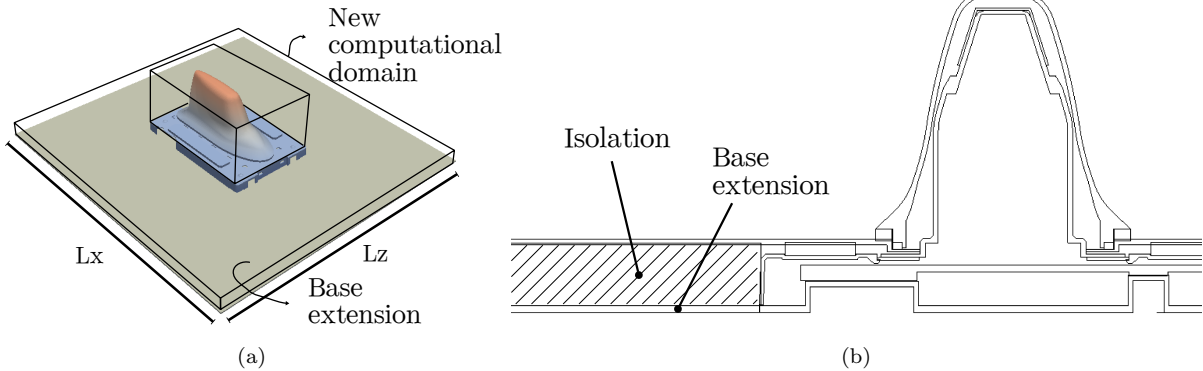

Figure 32: (a) New computational domain when the dissipator is extended and (b) side view of the extension and isolation geometries.

With this configuration, the junction temperatures are reduced considerably, obtaining the following values: $T_J^T = 117^oC$, $T_J^U = 118^oC$ and $T_J^P = 123^oC$. The losses to the bottom were increased with respect to the previous case, and distributed differently: $\dot{Q}_{Cond} = 6.86W$, $\dot{Q}_{Rad}^{Bottom} = 0.94W$ and $\dot{Q}_{Conv}^{Bottom} = 1.5W$. The losses by conduction are still the most important ones, but the convective and radiative losses are notoriously increased. This is due to the temperature distribution at the base, while in the previous case it was very uniform (almost adiabatic condition at the borders). In this case, the temperature decays from the chips
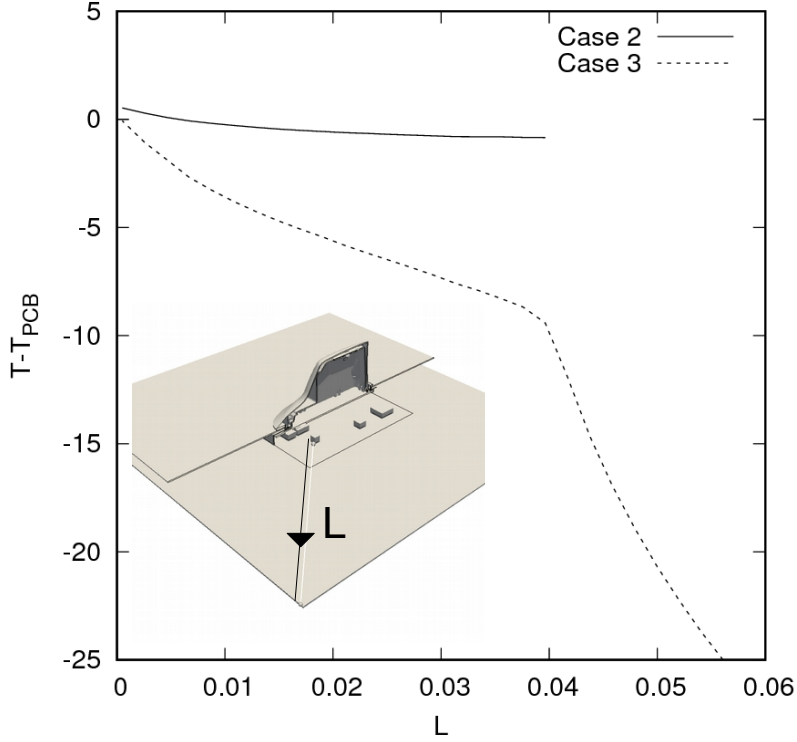
Figure 33: Temperature distribution along the base of the dissipator for cases 2 and 3.

region to the extension borders. Therefore, an important temperature difference between the PCB and base exists, which allows for part of the PCB heat to be dissipated by radiation and convection to the base. This can be observed in Figure 33, where the local temperature along the line indicated in the Figure minus the mean PCB temperature is plotted. In both cases the temperature close to the chip is very similar to the mean PCB temperature, but as L increases, the difference remains almost constant for Case 2 and strongly increases for Case 3.

Temperature maps are presented in Figures 34 and 35. As can be seen, the PCB temperature is slightly higher than the shell temperature, which reduces the heat losses to the top with respect to the previous cases: $\dot{Q}_{Rad}^{Top} = 0.9W$ and $\dot{Q}_{Conv}^{Top} = -0.2W$.

4.2.4. Case 4. Built-in dissipator extended with coarse aluminum

The last case simulated in this work is a variation from the previous case, modifying only the extension thickness to $d_{Al}^{ext} = 1mm$. This is not a viable design due to the quantity of aluminum that it requires, but its study gives an idea of the limits of using passive methods to dissipate the generated power. The huge increase of the extension thickness increments the fin efficiency reducing even more the temperature of the PCB, computing: $T_J^T = 108^oC$, $T_J^U = 108^oC$ and $T_J^P = 113^oC$.

The relatively low values of the temperature at the PCB makes it receive heat from the top of the domain: $\dot{Q}_{Rad}^{Top} = -0.3W$ and $\dot{Q}_{Conv}^{Top} = -2.7W$. This incoming extra heat from the top is dissipated to the bottom: $\dot{Q}_{Cond} = 10.82W$, $\dot{Q}_{Rad}^{Bottom} = 1.18W$ and $\dot{Q}_{Conv}^{Bottom} = 1.0W$.
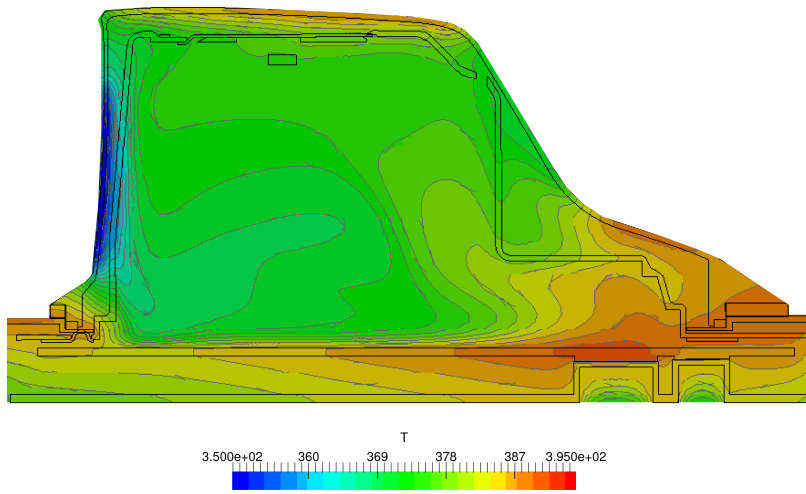
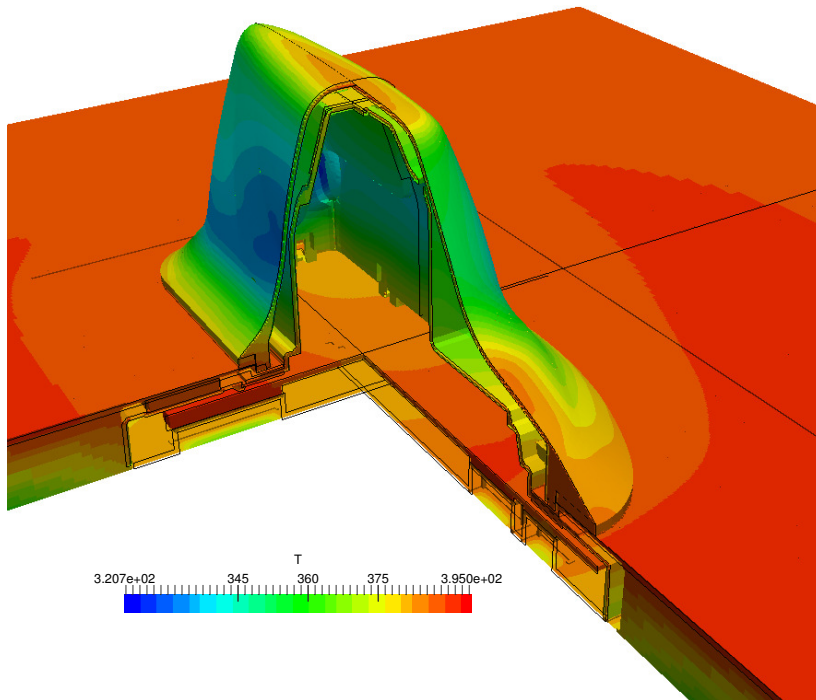Figure 34: Temperature contour plots of a side view in the middle of the domain for Case 3.

Figure 35: Temperature distribution in the surface of the solids parts for Case 3.

4.2.5. Comparison between cases and discussion

To summarize the obtained results, the temperatures of the electronic chips for each case are presented in Table 4 and in Figure 38. The horizontal lines in the Figure separates the different working modes for a common electronic chip: if the junction temperature is below $105^{o}C$, the component works normally. If it is over that value but under $130^{o}C$, the component works in the so-called downgraded mode, which consists of
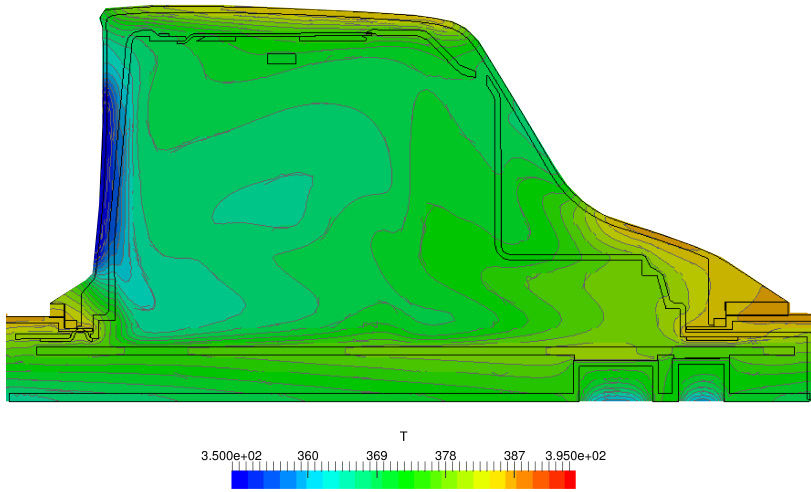
Figure 36: Temperature contour plots of a side view in the middle of the domain for Case 4.
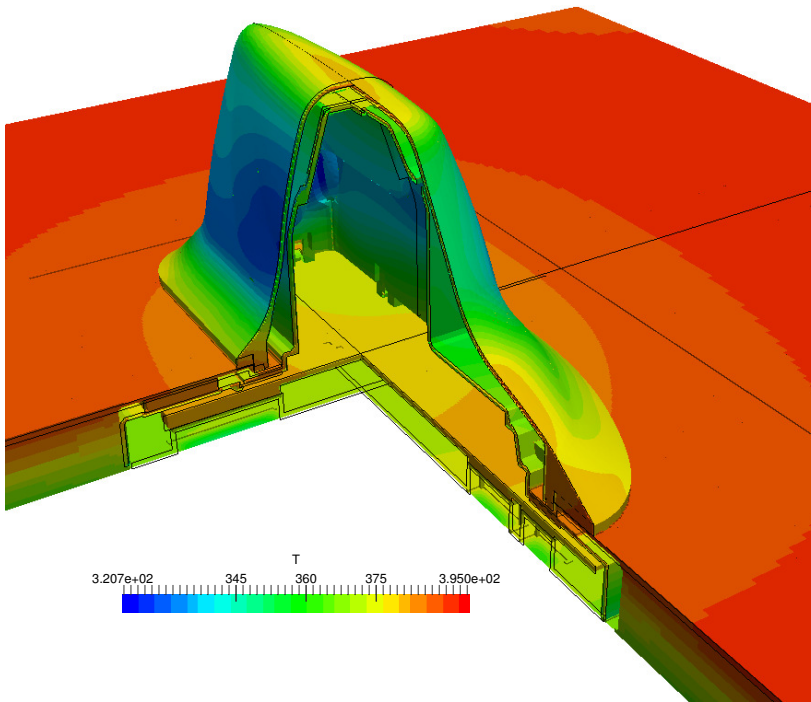

Figure 37: Temperature distribution in the surface of the solids parts for Case 4.

reducing the power by reducing the frequency. Finally, if the threshold of 130^oC is exceeded, the electronic component is damaged. As can be observed in Figure 38, each design is better compared to the previous one, but the aim of ensuring working temperatures in the normal mode is not achieved.

The heat losses of the PCB are summarized in Table 5. In each new design the PCB temperature is reduced thanks to the decrease of the global thermal resistance from the PCB to the interior of the car. This
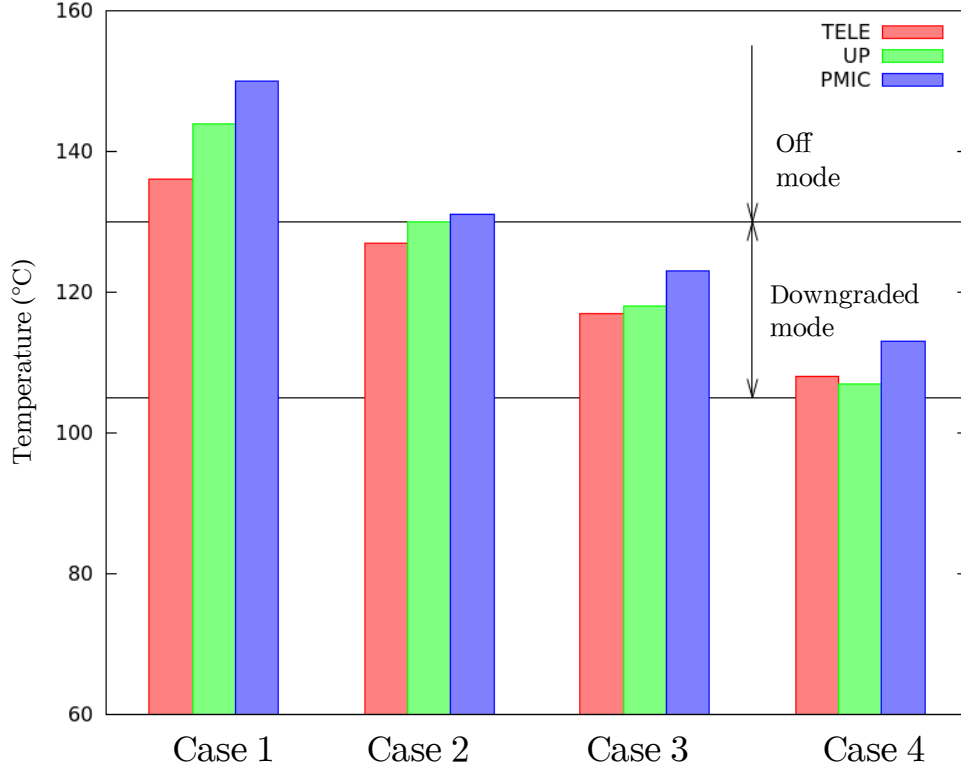
Figure 38: Comparison between cases of the Junction temperature at the different chips.

	TM $T_J^T(^oC)$	UP $T_J^U(^oC)$	PMIC $T_J^P(^oC)$
Case 1	136	144	150
Case 2	127	130	131
Case 3	117	118	123
Case 4	108	108	113

Table 4: Junction temperature at the different chips.

strategy allows the heat losses to the bottom to be enhanced in each new case, and the heat losses to the top to be reduced, to such an extent that in Case 4 the top region of the PCB is receiving heat from its surroundings.

Although the thermal requirements were not achieved in the new designs, the information provided by the simulations can be very useful for future steps in the development of the SAM. The idea of dissipating the heat to the interior of the car is in its limits, and a complementary strategy must be analyzed. For example, the lateral walls of the shell have a lower temperature than the PCB, even in Case 4, which could be used to reduce temperatures with new dissipators. The net radiation heat that the PCB receives from the shell and roof could be reduced by low-radiative painting in specific regions, according to the hot surfaces observed in the temperature maps obtained from the simulations. The impact of these ideas can be studied by new

simulations, and the new designs can be tested in normal conditions with the PCB working full-power.

	$\dot{Q}_{Rad}^{Top}$ (W)	$\dot{Q}_{Rad}^{Bottom}$ (W)	$\dot{Q}_{Conv}^{Top}$ (W)	$\dot{Q}_{Conv}^{Bottom}$ (W)	$\dot{Q}_{Cond}$ (W)
Case 1	1.8	4.5	0.5	2.0	1.2
Case 2	1.4	0.3	0.1	0.6	7.6
Case 3	0.9	0.94	-0.2	1.5	6.86
Case 4	-0.3	1.18	-2.7	1.0	10.82

Table 5: Heat losses of the PCB.

5. Conclusions

An immersed boundary method (IBM) to simulate conjugate heat transfer problems, including radiative surface exchange, was presented. The non-slip condition for the velocity field was imposed by the reconstruction of the solution using the discrete forcing approach [15] and modifying the Poisson equation to ensure no mass pass through the boundaries. The main purpose of that was to have a precise description of the mass flux in the vicinity of the immersed boundaries in order to compute an accurate advective term in the energy equation. The conjugate immersed boundary condition was introduced by an adaptation of the convective and diffusive operators in the cells intersected by the immersed boundary. The radiative exchange between surfaces was taken into account by incorporating a source term computed by solving the net radiation problem. The models were developed for generic meshes. The reconstruction procedures by linear interpolations used in momentum equation was formulated to work with any type of meshes. The modifications in the discretization of the Poisson and energy equations were also formulated for generic cells.

The validation and verification of the code was carried out through the simulation of three different test cases. First, an accuracy study was performed through the solution of the flow between two cylinders, considering the conduction inside the inner cylinder. A second-order of accuracy was obtained for velocity and temperature when the CHT problem was solved. When the radiative exchange between cylinders was considered, the order of accuracy for the temperature field was less than first order, which may be due to the dependency of the radiative heat transfer with the fourth power of the surface temperature. The second case were selected to test the approach proposed for the analysis of the Poisson equation. With this approach, the solution is improved in cases with big pressure gradients generated because of the presence of thin bodies. Finally, a two-dimensional case from the literature which considers conduction, convection and radiation was used. Even not necessary, an unstructured mesh was generated in order to have a more exigent non-body conformal discretization. Very good agreement with the results of the reference, which uses an accurate body-conformal methodology, was obtained.

A monolithic approach methodology has been proven to be successful in the solution of multi physics problems, resulting especially appropriate for engineering applications, where the combination of various heat-transfer mechanisms is frequent. By representing the solid-fluid interfaces using unstructured surface meshes, the method can be applied for all kinds of geometries. Moreover, the domain mesh generation process is simplified, allowing to simulate several configurations with the same domain discretization. The techniques were applied to study the thermal performance of Smart Antenna Module in the framework of a collaboration between CTTC and FICOSA INTERNACIONAL, S.A. First, an original configuration proposed by the company was simulated, where the hot body (PCB) is almost isolated from the cold parts (bottom surface and inclined sides of the shark cover). As was expected, the junction temperature of the

working chips were over the damage threshold. Three more configurations were then simulated. In each new case, an aluminum dissipator was included, in order to reduce the global thermal resistance between the PCB and the bottom. Despite the fact that the proposed configurations were not able to reduce the working temperature of the electronic component as much as was needed, the study was useful to determine the limits of the passive heat dissipation under the design limitations and to define new steps in the project. For example, the lateral walls of the shell have a lower temperature than the PCB, which could be used to reduce temperatures with new dissipators. The net radiation heat that the PCB receives from the shell and roof, could be reduced by low-radiative painting in specific regions, according to the hot surfaces observed in the temperature maps obtained from the simulations.

References

[1] O. Aydin, W. Yang, Natural convection in enclosures with localized heating from below and symmetrical cooling from sides, International Journal of Numerical Methods for Heat & Fluid Flow 10 (2000) 518–529.

[2] V. Panthalookaran, CFD-Assisted Optimization of Chimneylike Flows to Cool an Electronic Device, Journal of Electronic Packaging 132 (2010).

[3] R. Boukhanouf, A. Haddad, A CFD Analysis of an electronics cooling enclosure for application in telecommunication systems, Applied Thermal Engineering 30 (2010) 2426.

[4] S. G. Martyushev, M. A. Sheremet, Conjugate natural convection combined with surface thermal radiation in an air filled cavity with internal heat source, International Journal of Thermal Sciences 76 (2014) 51–67.

[5] S. G. Martyushev, M. A. Sheremet, Conjugate natural convection combined with surface thermal radiation in a three-dimensional enclosure with a heat source, International Journal of Heat and Mass Transfer 73 (2014) 340 – 353.

[6] I. V. Miroshnichenko, M. A. Sheremet, A. A. Mohamad, Numerical simulation of a conjugate turbulent natural convection combined with surface thermal radiation in an enclosure with a heat source, International Journal of Thermal Sciences 109 (2016) 172–181.

[7] A. Riaz, A. Basit, A. Ibrahim, A. Shah, M. A. Basit, A three-dimensional cfd and experimental study to optimize naturally air-cooled electronic equipment enclosure: Effects of inlet height, heat source position, and buoyancy on mean rise in temperature, Asia-Pacific Journal of Chemical Engineering 13 (2017) e2145.

[8] R. Mittal, G. Iaccarino, Immersed Boundary Methods, Annual Review of Fluid Mechanics 37 (2005) 239–261.

[9] C. S. Peskin, Flow patterns around heart valves: a numerical method., Journal of Computational Physics 10 (1972) 252–271.

[10] C. S. Peskin, D. M. McQueen, Modeling prosthetic heart valves for numerical analysis of blood flow in the heart, Journal of Computational Physics 37 (1980) 113–132.

[11] C. S. Peskin, D. M. McQueen, Cardiac fluid dynamics, Critical Reviews in Biomedical Engineering 20 (1992) 451–459.

[12] D. M. McQueen, C. S. Peskin, Shared-Memory Parallel Vector Implementation of the Immersed Boundary Method for the Computation of Blood Flow in the Beating Mammalian Heart, The Journal of Supercomputing 236 (1997) 213–236.

[13] M.-C. Lai, C. S. Peskin, An Immersed Boundary Method with Formal Second-Order Accuracy and Reduced Numerical Viscosity, Journal of Computational Physics 160 (2000) 705–719.

[14] J. Mohd-Yusof, Flow patterns around heart valves: A numerical method, Center for Turbulence Research Annual Research Briefs (1997) 317–327.

[15] E. Fadlun, R. Verzicco, P. Orlandi, J. Mohd-Yusof, Combined Immersed-Boundary Finite-Difference Methods for Three-Dimensional Complex Flow Simulations, Journal of Computational Physics 161 (2000) 35–60.

[16] E. Balaras, Modeling complex boundaries using an external force field on fixed Cartesian grids in large-eddy simulations, Computers and Fluids 33 (2004) 375–404.

[17] J. Yang, E. Balaras, An embedded-boundary formulation for large-eddy simulation of turbulent flows interacting with moving boundaries, Journal of Computational Physics 215 (2006) 12–40.

[18] J. Kim, D. Kim, H. Choi, An Immersed-Boundary Finite-Volume Method for Simulations of Flow in Complex Geometries, Journal of Computational Physics 171 (2001) 132–150.

[19] S. Majumdar, G. Iaccarino, P. Durbin, RANS solvers with adaptive structured boundary non-conforming grids, Annual Research Briefs (2001) 353–366.

[20] Y.-H. Tseng, J. H. Ferziger, A ghost-cell immersed boundary method for flow in complex geometry, Journal of Computational Physics 192 (2003) 593–623.

[21] J. Kim, H. Choi, An immersed-boundary finite-volume method for simulation of heat transfer in complex geometries, KSME International Journal 18 (2004) 1026–1035.

[22] Z. Wang, J. Fan, K. Luo, K. Cen, Immersed boundary method for the simulation of flows with heat transfer, International Journal of Heat and Mass Transfer 52 (2009) 4510–4518.

[23] J. R. Pacheco, A. Pacheco-Vega, T. Rodic, R. E. Peck, Numerical Simulations of Heat Transfer and Fluid Flow Problems Using an Immersed-Boundary Finite-Volume Method on NonStaggered Grids, Numerical Heat Transfer, Part B: Fundamentals 48 (2005) 1–24.

[24] D. Pan, An Immersed Boundary Method on Unstructured Cartesian Meshes for Incompressible Flows with Heat Transfer, Numerical Heat Transfer, Part B: Fundamentals 49 (2006) 277–297.

[25] A. Pacheco-Vega, J. R. Pacheco, T. Rodic, A General Scheme for the Boundary Conditions in Convective and Diffusive Heat Transfer With Immersed Boundary Methods, Journal of Heat Transfer 129 (2007) 1506.

[26] A. Gilmanov, S. Acharya, A computational strategy for simulating heat transfer and flow past deformable objects, International Journal of Heat and Mass Transfer 51 (2008) 4415–4426.

[27] C. Shu, W. W. Ren, W. M. Yang, Novel immersed boundary methods for thermal flow problems, International Journal of Numerical Methods for Heat & Fluid Flow 23 (2013) 124–142.

[28] G. Iaccarino, S. Moreau, Natural and Forced Conjugate Heat Transfer in Complex Geometries on Cartesian Adapted Grids, Journal of Fluids Engineering 128 (2006) 838.

[29] S. Kang, G. Iaccarino, F. Ham, DNS of buoyancy-dominated turbulent flows on a bluff body using the immersed boundary method, Journal of Computational Physics 228 (2009) 3189–3208.

[30] K. Nagendra, D. K. Tafti, K. Viswanath, A new approach for conjugate heat transfer problems using immersed boundary method for curvilinear grid based solvers, Journal of Computational Physics 267 (2014) 225–246.

[31] N. Sato, S. Takeuchi, T. Kajishima, M. Inagaki, N. Horinouchi, A consistent direct discretization scheme on Cartesian grids for convective and conjugate heat transfer, Journal of Computational Physics 321 (2016) 76–104.

[32] P. A. Galione, O. Lehmkuhl, J. Rigola, A. Oliva, Fixed-grid numerical modeling of melting and solidification using variable thermo-physical properties - Application to the melting of n-Octadecane inside a spherical capsule, International Journal of Heat and Mass Transfer 86 (2015) 721–743.

[33] H. S. Udaykumar, R. Mittal, P. Rampunggoon, A. Khanna, A Sharp Interface Cartesian Grid Method for Simulating Flows with Complex Moving Boundaries, Journal of Computational Physics 174 (2001) 345–380.

[34] T. Ye, R. Mittal, H. Udaykumar, W. Shyy, An Accurate Cartesian Grid Method for Viscous Incompressible Flows with Complex Immersed Boundaries, Journal of Computational Physics 156 (1999) 209–240.

[35] J. H. Seo, R. Mittal, A sharp-interface immersed boundary method with improved mass conservation and reduced spurious pressure oscillations, Journal of Computational Physics 230 (2011) 7347–7363.

[36] S. Ergin, Surface radiation with conduction and natural convection in a two-floor enclosure, Energy and Buildings 32 (2000) 57–70.

[37] A. K. Sharma, K. Velusamy, C. Balaji, S. P. Venkateshan, Conjugate turbulent natural convection with surface radiation in air filled rectangular enclosures, International Journal of Heat and Mass Transfer 50 (2007) 625–639.

[38] S. M. Sawant, C. Gururaja Rao, Conjugate mixed convection with surface radiation from a vertical electronic board with multiple discrete heat sources, Heat and Mass Transfer/Waerme- und Stoffuebertragung 44 (2008) 1485–1495.

[39] H. F. Nouanégué, E. Bilgen, Heat transfer by convection, conduction and radiation in solar chimney systems for ventilation of dwellings, International Journal of Heat and Fluid Flow 30 (2009) 150–157.

[40] O. Antepara, O. Lehmkuhl, R. Borrell, J. Chiva, A. Oliva, Parallel adaptive mesh refinement for large-eddy simulations of turbulent flows, Computers and Fluids 110 (2015) 48–61.

[41] TermoFluids S.L., www.termofluids.com, 2016.

[42] M. Burns, StereoLithography Interface Specification, Technical Report, 3D System Inc., Valencia, 1988.

[43] R. W. C. P. Verstappen, A. E. P. Veldman, Direct numerical simulation of turbulence at lower costs, J. of Engineering Mathematics 32 (1997) 143–159.

[44] F. X. Trias, O. Lehmkuhl, A Self-Adaptive Strategy for the Time Integration of Navier-Stokes Equations, Numerical Heat Transfer, Part B: Fundamentals 60 (2011) 116–134.

[45] M. Meyer, A. Devesa, S. Hickel, X. Y. Hu, N. A. Adams, A conservative immersed interface method for Large-Eddy Simulation of incompressible flows, Journal of Computational Physics 229 (2010) 6300–6317.

[46] R. Mittal, H. Dong, M. Bozkurttas, F. M. Najjar, A. Vargas, A. von Loebbecke, A versatile sharp interface immersed boundary method for incompressible flows with complex boundaries, Journal of Computational Physics 227 (2008) 4825–4852.

[47] M. F. Modest, Radiative Exchange Between Gray, Diffuse Surfaces, in: Radiative Heat Transfer, 2013, pp. 160–196.

[48] M. F. Modest, The Monte Carlo Method for Surface Exchange, in: Radiative Heat Transfer, 2013, pp. 247–266.

[49] T. Miyanaga, Y. Nakano, Radiation heat transfer in three-dimensional closed space including diffuse and specular surfaces, Heat Transfer - Asian Research 32 (2003) 108–129.

[50] Y. Saad, M. H. Schultz, GMRES: A Generalized Minimal Residual Algorithm for Solving Nonsymmetric Linear Systems, SIAM Journal on Scientific and Statistical Computing 7 (1986) 856–869.

[51] E. P. Roberts, A numerical and experimental study of transition processes in an obstructed channel flow, Journal of Fluid Mechanics 260 (1994) 185–209.

[52] E. Martinez-Ortigosa, R. Quintero-Illera, L. Tantiña-Cuni, A. Sanz-Arronte, P. Mogas-Fabre, Antenna for motor vehicles and assembling method, 2017.

[53] P. Berdahl, R. Fromberg, The thermal radiance of clear skies, Solar Energy 29 (1982) 299–314.

[54] P. Berdahl, M. Martin, Emissivity of clear skies, Solar Energy 32 (1984) 663–664.

[55] S. W. Churchill, H. H. S. Chu, Correlating equations for laminar and turbulent free convection from a vertical plate, International Journal of Heat and Mass Transfer 18 (1975) 1323–1329.

[56] A. Ede, An Introduction to Heat Transfer Principles and Calculations, Oxford University Press, London, 1967.